Stress-Induced Chemical Detection Using Flexible Metal-Organic Frameworks

Mark D. Allendorf, Ronald J.T. Houk, Leanne Andruszkiewicz, A. Alec Talin, J. Pikarsky, A. Choudhury, Kenneth A. Gall, Peter J. Hesketh

Approved for public release; further dissemination unlimited.

Sandia National Laboratories

Stress-Induced Chemical Detection Using Flexible Metal-Organic Frameworks

Mark D. Allendorf[1], Ronald J.T. Houk[1], Leanne Andruszkiewicz[2], A. Alec Talin[3], J. Pikarsky[2], A. Choudhury[2], Kenneth A. Gall[2], Peter J. Hesketh[2]

[1]Sandia National Laboratories, Livermore, CA 94551-0969. [2]School of Mechanical Engineering, Georgia Institute of Technology, Atlanta, GA 30331. [3]National Institute of Standards & Technology, 100 Bureau Dr. Gaithersburg, MD 20899.

Abstract

In this work we demonstrate the concept of stress-induced chemical detection using metal-organic frameworks (MOFs) by integrating a thin film of the MOF HKUST-1 with a microcantilever surface. The results show that the energy of molecular adsorption, which causes slight distortions in the MOF crystal structure, can be efficiently converted to mechanical energy to create a highly responsive, reversible, and selective sensor. This sensor responds to water, methanol, and ethanol vapors, but yields no response to either N_2 or O_2. The magnitude of the signal, which is measured by a built-in piezoresistor, is correlated with the concentration and can be fitted to a Langmuir isotherm. Furthermore, we show that the hydration state of the MOF layer can be used to impart selectivity to CO_2. We also report the first use of surface-enhanced Raman spectroscopy to characterize the structure of a MOF film. We conclude that the synthetic versatility of these nanoporous materials holds great promise for creating recognition chemistries to enable selective detection of a wide range of analytes. A force field model is described that successfully predicts changes in MOF properties and the uptake of gases. This model is used to predict adsorption isotherms for a number of representative compounds, including explosives, nerve agents, volatile organic compounds, and polyaromatic hydrocarbons. The results show that, as a result of relatively large heats of adsorption (> 20 kcal mol^{-1}) in most cases, we expect an onset of adsorption by MOF as low as 10^{-6} kPa, suggesting the potential to detect compounds such as RDX at levels as low as 10 ppb at atmospheric pressure.

ACKNOWLEDGMENTS

CONTENTS

FIGURES

TABLES

6

1. INTRODUCTION

Real-time, compact, and inexpensive chemical detectors are highly desirable for several important Sandia missions, including embedded surveillance of nuclear weapons, explosives and CWMD detection, water-quality monitoring, and personal exposure monitors (PEM). PEM are possibly the most demanding of these applications and are needed to provide the accurate knowledge of exposure levels required to understand the complex interplay between genes and environmental factors such as ozone, PAH, VOCs, and pesticides. In each of these applications the available technologies lack the essential combination of sensitivity, portability, and low cost. Lack of specificity and ability to measure multiple analytes is also a problem. Although detection systems with both time resolution and the requisite sensitivity exist, such as mass spectrometry, flame ionization, fluorescence, and chemiluminescence, portable, low-cost and/or compact versions are not available and many require a front-end separation technology such as gas chromatography. Interdisciplinary approaches to developing new materials and device concepts are needed to enable real-time monitoring of extremely low concentrations of multiple toxicants simultaneously in a non-obtrusive manner.
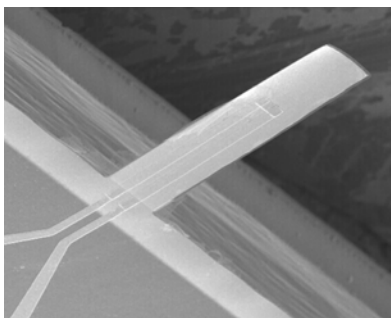
Figure 1. Georgia Tech microcantilever design with built-in piezoresistive stress sensor.

Static microcantilever (SMC) detectors, which detect by adsorption-induced bending, offer the potential for high-sensitivity multiplexed chemical detection and low-cost, portable hardware. Static designs outperform resonant-beam designs and have sensitivities superior to quartz crystal microbalances, SAW transducers, and conventional piezoelectric gravimetric sensors. They also have very low power requirements and can incorporate a built-in piezoresistive stress sensor, eliminating the need for on-board optical monitoring schemes that substantially increase complexity and cost. CMOS-compatible fabrication enables low cost integration into arrays of sensors. Finally, they eliminate fluid damping effects, enabling liquid-phase measurements. The design developed by our Georgia Tech (GT) partners (see below and Fig. 1) is the most sensitive reported to date, with a limit of detection of 0.04 mN/m, equivalent to a deflection of only 5 nm. However, to be useful for the demanding applications listed above, sub-ppb sensitivities are required, equivalent to picomolar concentrations in water and femtomolar concentrations in air. Recognition chemistries are needed that can induce differential stress in the cantilever while simultaneously providing specificity to identify a broad range of analytes.

The objectives of this project were to discover new recognition chemistries based on novel nanoporous coordination polymers (CP) and integrate them with SMCs to create a new generation of versatile sensors with unprecedented sensitivity and selectivity. Adsorbate-induced

structural flexibility is exhibited by nanoporous CP, such as the ultrahigh surface-area materials known as metal organic frameworks (MOF), suggesting a novel device functionalization route that can provide very high sensitivity with structural and chemical tailorability for selective detection. The unit cell dimensions of CP can vary by as much as 10% when molecules are adsorbed within their pores (Uemura et al. *J. Sol. State Chem.,* 2005). Mechanical coupling to a MC would therefore induce easily detectable stresses. Our calculations indicate that 1-µm thick layers of a CP known as IRMOF-1 would lead to measurable tip deflections corresponding to *femtomolar* concentrations. Importantly, the crystalline nature of CP allows sophisticated modeling approaches to be used to establish the connection between the chemistry within their pores and the mechanical stresses induced by adsorption, enabling a fully rational design process to be implemented. In addition, due to their high surface areas ($> 4,000$ m^2/g in some cases), gas sorption rivaling conventional gas cylinders is possible. Thus, CP can also function as preconcentrators, enabling increased detection sensitivity. At the outset of this LDRD project, the integration of CPs with devices was entirely unexplored and there were only a handful of publications that addressed growth of CP on surfaces, creating the opportunity for ground-breaking scientific advances.

2. STRESS-INDUCED CHEMICAL DETECTION USING FLEXIBLE METAL-ORGANIC FRAMEWORKS[*]

Metal-organic frameworks (MOFs) are currently attracting considerable attention because their tailorable nanoporosity and ultrahigh surface areas make them ideal candidates for a variety of sensing applications. Although this potential is often noted, to date there are no reports of MOFs serving as a component of a functioning device. An intriguing aspect of these materials is that they exhibit adsorbate-induced structural flexibility.[1,2] The unit cell dimensions of some MOFs can vary by as much as 10% when molecules are absorbed within their pores.[3] This suggests a novel transduction mechanism in which distortions in a MOF thin film create stress at the interface with a second material. Such stresses can be measured by depositing a MOF film on the surface of a static microcantilever. In a device of this type, stress at the cantilever surface results in bending that can be detected optically or by means of a built-in piezoresistive sensor.[4] Clearly, the sensitivity of such a device depends upon strong chemical bonding between the MOF and the surface, so that the stress is effectively transmitted to the cantilever. It also depends on the stiffness of the MOF. We recently reported the elastic properties of IRMOF-1 and find that, although the solvated and desolvated unit cell dimensions differ by only 0.8% , the Young's modulus of this material[5] is sufficiently high to create easily measurable stresses. Here, we demonstrate the concept of stress-induced chemical detection by integrating a thin film of the MOF HKUST-1[6] with a microcantilever surface. The results show that the energy of molecular adsorption within a porous MOF can be efficiently converted to mechanical energy to create a highly responsive, reversible, and selective sensor.

The choice of HKUST-1, a MOF composed of Cu(II) ions linked by benzenetricarboxylate (BTC) ligands $[Cu_3BTC_2(H_2O)_3]_n$, is a logical one for several reasons. First, methods of growing HKUST-1 on surfaces have recently been reported.[7,8] The resulting coatings are dense and reproducible, in contrast with IRMOF-1, whose thickness, uniformity, and microstructure we find difficult to control with reported methods.[9] Second, the cubic unit cell of this MOF undergoes a small (0.12 Å) but significant contraction upon removal of the two axially coordinated water molecules.[10] Finally, the availability of open coordination sites in the dehydrated version of HKUST-1 suggests that analyte-specific adsorption may be possible. Indeed, adsorption isotherms for a variety of gases have been reported.[11]

The platform for our investigation is a 10-microcantilever array, in which each cantilever incorporates a built-in piezoresistive sensor for stress-based detection.[12] HKUST-1 layers for gas testing were deposited on gold-coated microcantilevers using the step-by-step method of Shekha et al.[8] We find this can be accomplished using the single-step method of Biemmi et al. as well.[7] Both methods use an intervening thiol-based self-assembled monolayer (SAM) on gold to attach the MOF to the substrate. Certain cantilevers were physically masked to prevent gold deposition and thus MOF growth, allowing them to serve as a reference. MOF growth was initiated by immersing the entire array sequentially in solutions of Cu(OAc)₂ and BTC in EtOH. A series of

20 immersion steps yields an average film thickness of ~100 nm, based on comparison with a macroscopic substrate subjected to the same procedure.
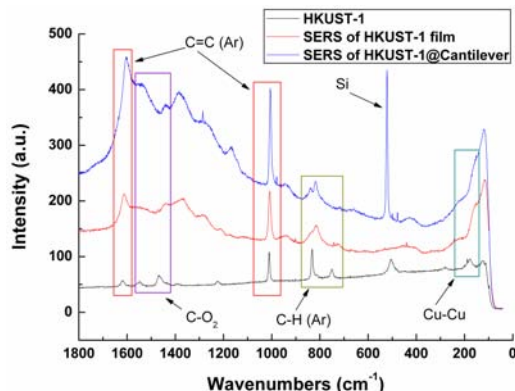
Figure 2. Verification of HKUST-1 on the microcantilever using SERS. Blue: SERS spectrum of HKUST-1 on a microcantilever. Red: SERS spectrum of an HKUST-1 film on a macroscopic substrate. Black: unenhanced Raman of a thick HKUST-1 layer used as a reference. Peaks labeled C-H(Ar) correspond to out-of-plane aromatic C-H bends.

The microcantilever is too small to characterize by standard methods, such as x-ray diffraction (XRD), which could verify that HKUST-1 is present on the surface. Energy dispersive x-ray spectroscopy established the presence of copper and carbon in the film,[13] but the large penetration depth interferes with determination of the elemental composition. However, we find that micro-surface-enhanced Raman spectroscopy (μSERS) is a viable method for probing MOF films on microcantilevers. This method, previously unreported for MOF characterization, has a spatial resolution in our instrument of 2.0 μm^2. Large enhancement factors were achieved by evaporating silver onto the microcantilever (~2.5 nm equivalent). The resulting spectrum (Fig. 1, blue) is almost identical to that obtained from an HKUST-1 layer of similar thickness deposited on a macroscopic Au-coated silicon substrate (Fig. 1, red).[13] The unenhanced μ-Raman spectrum of a thick reference film (i.e., without the Ag layer; Fig. 1, black), whose composition was validated by comparing with the reported Raman spectrum[10] and XRD[6] of bulk HKUST-1, displays the same characteristic vibrational modes. Importantly, we obtain essentially the same SERS spectrum regardless of the surface morphology of the MOF film. Highly crystalline microstructures with clearly identifiable cube-octahedral shapes were obtained in some cases, while in others the surface had an amorphous appearance, but is likely highly nanocrystalline. Although the reasons for this are unclear, various morphologies are known to form as a result of minor changes in synthetic procedures, such as the degree of agitation during growth.[11]
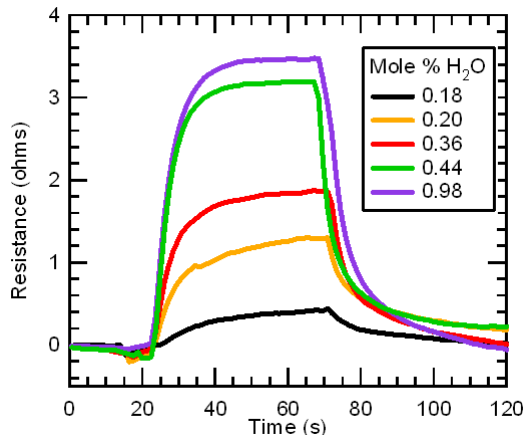
Figure 3. Temporal response of the cantilever piezoresistive sensor to water vapor diluted in N_2 (room temperature, 1 atm).

Since HKUST-1 has two exchangeable coordination sites, which are occupied by water molecules in the as-synthesized form, we measured the cantilever response in both the hydrated and dehydrated states of the MOF film. The latter was prepared by heating the cantilever using a DC voltage across the piezoresistor. A two-hour flow of dry N_2 at 50ºC is sufficient to remove the coordinated water, as shown by a color change from blue to purple in bulk samples subjected to this procedure.

In its hydrated state the MOF-coated microcantilever responds rapidly and reversibly to gas-phase H_2O, MeOH, and EtOH. For example, the time-dependent responses to H_2O are shown in Fig. 2. Easily measurable resistance changes relative to the reference sensor are generated within 500 ms (our shortest measurement interval), in contrast with uncoated cantilevers, which respond only minimally due to imperfect matching with the reference cantilever. No response to N_2, O_2, or CO_2 is observed. Upon replacement of the analyte gas with dry N_2, the signal decays exponentially with a time constant of ~10 s. A fit of the H_2O resistance to a Langmuir isotherm agrees reasonably well with a reported 0–3 mbar isotherm[11] and yields a saturated resistance of 7.0 ohms, which we predict[13] corresponds to a change in the HKUST-1 lattice parameter of $0.016 \pm 0.002\%$. XRD indicates a lattice expansion of 0.45% upon rehydration,[10] indicating that the MOF-cantilever interface is not completely rigid. This is reasonable and is most likely due to the SAM interface, film polycrystallinity, and incomplete coverage of the cantilever surface by the MOF layer.

A significant finding is that the sensor responds to CO_2 only when the MOF layer is dehydrated (Fig. 3 inset)]. New infrared bands assigned to CO_2 coordinated at axial Cu(II) sites suggest this is the cause of the sensor response.[14] The response is weaker than that induced by H_2O, consistent with the isotherms for these gases.[11] In contrast, the H_2O, MeOH, and EtOH responses are little affected by baking the sensor, suggesting that these signals are primarily due to adsorption on MOF pore surfaces and consistent with experiments indicating that fully hydrated HKUST-1 contains as much as 40 wt% water.[6,11] Thus, it appears that physisorbed molecules capable of hydrogen bonding generate sufficient interfacial stress to be detected, while weakly

interacting gases such as CO_2 must coordinate to the Cu(II) ions to be detected. Therefore, detection selectivity can be achieved by controlling the hydration state of the axial Cu(II) sites.
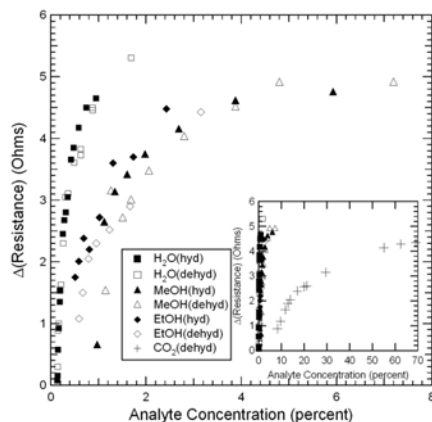
Figure 4. Resistance change versus analyte concentration expressed as a percentage of the total gas flow (balance N_2) at 298 K and 1 atm.

Our results indicate that MOFs can be effective recognition chemistries for a variety of gases. Since the adsorption-induced distortions in HKUST-1 are likely quite small, we expect that higher sensitivities can be achieved using MOFs exhibiting greater structural flexibility. Although the current device is far from optimized, sensitivity to alcohols and CO_2 and insensitivity to N_2 and O_2 suggest that this MOF might be useful in breath analysis if H_2O is removed prior to testing.

1.   Fletcher, A. J.; Thomas, K. M.; Rosseinsky, M. J. *J. Sol. State Chem.* **2005**, *178*, 2491.
2.   Uemura, K.; Matsuda, R.; Kitagawa, S. *J. Sol. State Chem.* **2005**, *178*, 2420.
3.   Serre, C.; Mellot-Draznieks, C.; Surblé, S.; Audebrand, N.; Filinchuk, Y.; Férey, G. *Science* **2007**, *315*, 1828.
4.   Goeders, K. M.; Colton, J. S.; Bottomley, L. A. *Chem. Rev.* **1997**, *108*, 522.
5.   Bahr, D. F.; Reid, J. A.; Mook, W. M.; Bauer, C. A.; Stumpf, R.; Skulan, A. J.; Moody, N. R.; Simmons, B. A.; Shindel, M. M.; Allendorf, M. D. *Phys. Rev. B* **2007**, 76, 184106.
6.   Chui, S. S.-Y.; Lo, S. M.-F.; Charmant, J. P. H.; Orpen, A. G.; Williams, I. D. *Science* **1999**, *283*, 1148.
7.   Biemmi, E.; Scherb, C.; Bein, T. *J. Am. Chem. Soc.* **2007**, *129*, 8054.
8.   Shekhah, C.; Wang, H.; Kowarik, S.; Schreiber, F.; Paulus, M.; Tolan, M.; Sternemann, C.; Evers, F.; Zacher, D.; Fischer, R. A.; Woll, C. *J. Am. Chem. Soc.* **2007**, *129*, 15118.
9.   Hermes, S.; Zacher, D.; Baunemann, A.; Wöll, C.; Fischer, R. A. *Chem. Mater.* **2007**, *19*, 2168.
10.   Prestipino, C.; Regli, L.; Vitillo, J. G.; Bonino, F.; Damin, A.; Lamberti, C.; Zecchina, A.; Solari, P. L.; Kongshaug, K. O.; Bordiga, S. *Chem.Mater.* **2006**, *18*, 1337.
11.   Wang, Q. M.; Shen, D.; Buulow, M.; Lau, M. L.; Deng, S.; Fitch, F. R.; Lemcoff, N. O.; Semanscin, *J. Microporous Mesoporous Mat.* **2002**, *55*, 217.

12. Choudhury, A.; Hesketh, P. J.; Thundat, T.; Hu, Z. Y. J. Micromech. Microeng. 2007, 17, 2065.
13. See the Supporting Information for details.
14. Bordiga, S.; Regli, L.; Bonino, F.; Groppo, E.; Lamberti, C.; Xiao, B.; Wheatley, P. S.; Morris, R. E.; Zecchina, A. *Phys. Chem. Chem. Phys.* **2007**, *9*, 2676.

[Blank page following section.]

3. FORCE FIELD VALIDATION FOR MOLECULAR DYNAMICS SIMULATIONS OF IRMOF-1 AND OTHER ISORETICULAR ZINC CARBOXYLATE COORDINATION POLYMERS[†]

3.1 Introduction

Metal organic frameworks (MOFs) are a diverse class of coordination polymers in which metal ions are connected to each other through bridging organic "linker" molecules that coordinate to the metal centers.[1,2] Although not microporous by definition, the MOFs attracting the most attention recently have robust, open-framework structures with sufficient structural stability to allow them to maintain their porosity upon removal of solvent. The isoreticular series of zinc- and copper-based IRMOF (isoreticular metal-organic framework) compounds developed by Yaghi et al.[3] and the MIL compounds developed by Férey et al.[4,5] are of particular interest because of their potential for rational design of nanoporous materials, enabled by the inherent synthetic versatility of the linker molecule. While the discovery of exceptional gas sorption properties by MOFs has been mostly adventitious, several recent attempts to rationally design their properties for specific applications, such as hydrogen[6-8] or methane[9] storage and CO_2 sequestration[10] have been reported.

Although a seemingly vast array of possibilities for creating MOFs with specific properties would seem to exist, neither the properties resulting from the choice of a particular linker, nor the ability to synthesize a MOF from it can be considered a certainty. Thus, there is an important role for theoretical methods that can predict properties such as molecular diffusion and adsorption, enabling the most promising candidates to be identified prior to launching a potentially time-consuming synthetic effort. Atomistic methods, such as molecular dynamics and Monte Carlo techniques, are particularly attractive for this purpose, due to their ability to treat a wide variety of related chemical systems coupled with relatively high computational efficiency for large-scale systems.[11] The prototypical MOF compound in computational studies has been IRMOF-1 (also known as MOF-5), which consists of Zn_4O vertices connected by benzene dicarboxylate (BDC or terphthalate) linkers. To date, a number of studies have been reported, focusing on hydrogen,[12-17] methane,[16,18-21] CO_2,[16,21,22] hydrocarbons,[16,19,21,23,24] and inert gases.[16,25,26]

These previous investigations employed standard force fields to model the interaction between the MOF and molecules within its pores, such as the universal force field,[27] DREIDING force field,[28] and OPLS force field,[29] or by custom optimization of Lennard-Jones potentials.[23] In all cases, the atoms within the MOF were not allowed to move during the simulation. It is apparent, however, that MOFs are structurally flexible and can exhibit substantial changes in unit cell parameters upon adsorption or desorption of guest molecules.[30,31] For example, Cussen *et al.* present evidence for dynamic flexibility in a nickel-pyridine MOF that absorbs toluene even though its pore dimensions are too small to admit this molecule.[32] Fixed-atom force fields obviously cannot capture these effects. It also clear that the parameterization of these existing

force fields is not always well-suited to the description of MOFs. In some cases allowing the empty framework to relax results in unreasonably short bond distances,[32] while in others diffusion constants are significantly overpredicted.[24]

One approach to these problems is the "flexible," but still fully bonded, force field developed by Schmid and coworkers,[24,33] who parameterized the MM3 force field to account for interactions with the Zn_4O clusters in IRMOF-1. This model successfully predicts the IRMOF-1 structure and yields vibrational frequencies in reasonable agreement with the predictions of density functional theory (DFT).[33] It is also encouraging that the benzene self-diffusion constant obtained from MD calculations is within ~30% of the value measured by NMR.[24] More recently, another fully bonded, but flexible force field for IRMOF-1 was used to calculate the phonon thermal conductivity and vibrational power spectra of this MOF using molecular dynamics.[34]

An additional limitation of fully bonded force fields, whether or not the atoms are fixed, is that they cannot be used to probe framework reactivity with respect to either adsorbates or solvent environments. To address this problem, as well as the need for structural flexibility, we recently reported a non-bonded force field for IRMOF-1 that reproduces the crystal structure of this compound.[35] This model for zinc-carboxylate MOFs was calibrated by comparison with both the reported x-ray crystal structure for IRMOF-1[9] and DFT calculations of ZnO.[36] As a result, our force field correctly predicts the structure of IRMOF-1, in contradiction to the statements in refs 21 and 24.[37] Molecular dynamics (MD) simulations of the interaction of adsorbed water in IRMOF-1 using our non-bonded force field predict framework collapse above a critical water concentration, in qualitative agreement with experiment.[38,39] Following our nonbonded approach, Dubbeldam et al.[21] also used a hybrid force field for simulations of several Zn-based IRMOFs. In addition to structural comparisons, these authors used adsorption isotherms for CO_2 and CH_4 in the parameter fitting process. As a result, that work demonstrates that a force field based on our non-bonded approach can correctly predict measured adsorption isotherms.[21]

In this paper, we present a detailed validation of the non-bonded force field initially described in ref 35, demonstrating its ability to accurately predict a number of important properties of an IRMOF. Specifically, we describe MD simulations of the dependence of the IRMOF-1 lattice parameter on temperature and guest molecule and show that these agree well with previously reported experimental results. In addition, we predict the total energy of the IRMOF-1 unit cell as a function of lattice constant as well as its pressure dependence, finding that these are in good agreement with the predictions of first-principles periodic DFT/local density approximation (LDA) calculations. In what we believe is a particularly rigorous test of the force field, we obtain vibrational frequencies from atomic power spectra. As we show below, the model correctly predicts the vibrational motion of ZnO_4 tetrahedra and 180° rotations of phenyl groups in IRMOF-1. Finally, calculations of the activation energy for benzene diffusion at low loading agree well with the prediction of Amirjalayer et al. using their MM3-based force field.[24] The good agreement with the results of both experiments and first-principles theory establishes the non-bonded approach as the foundation for a generalized force field for zinc-carboxylate IRMOFs.

3.2 Simulation Methods

Force field parameters for IRMOF-1 have been described previously[35] and will only be summarized here. Parameters for the BDC linker atoms were adapted from the CVFF force field[40] with slight modifications as discussed previously.[35] CVFF is a general purpose force field used primarily for organic molecules. It's transferability to a range of organic compounds makes it attractive for use in a general force field for MOFs. Nonbonded potential energy interactions E_{ij} between atoms i and j separated by a distance r were calculated according to

$$E_{ij} = \frac{q_i q_j}{r} + 4\varepsilon_{ij}\left[\left(\frac{\sigma_{ij}}{r}\right)^{12} - \left(\frac{\sigma_{ij}}{r}\right)^{6}\right] \tag{1}$$

where $\sigma_{ij} = \sqrt{\sigma_i \sigma_j}$ and $\varepsilon_{ij} = \sqrt{\varepsilon_i \varepsilon_j}$ represent the van der Waals radius and energy well depth for the atomic pair. These parameters are given in Table 1. Intramolecular interactions (bond stretch, angle bend, dihedral angle, improper angle) for BDC atoms were also adapted from CVFF[40] with minor changes[35] as summarized in Table 2. The force field includes no intramolecular interactions for Zn-O_{cent} and Zn-O_{carb} pairs. Instead, only nonbonded interactions (eqn 1) were used to allow for maximum flexibility on the Zn_4O tetrahedra. Parameters for IRMOF-1 were determined by manual fitting to obtain good agreement with published structural data for pure IRMOF-1 (i.e., without adsorbed guest molecules). Parameters for guest molecules were taken from CVFF[40] without modification and were treated with full flexibility. These parameters were not optimized for bulk liquid properties of these guest molecules. Geometric mixing rules were used to calculate host-guest van der Waals parameters.

Table 1. Force Field Parameters (atomic charge q and Van der Waals parameters σ and ε for Nonbonded Interactions in IRMOF-1 and Guests.

atom type[a]	description	q (e)	σ (Å)	ε (kJ·mol^{-1})
Zn	zinc	1.200	2.3110	0.006
O_{cent}	inorganic oxygen	−1.200	3.0882	3.548
O_{carb}	carboxylate oxygen	−0.600	2.9861	3.548
C_{carb}	carboxylate carbon	0.600	3.6170	0.619
C_{phenyl}	phenyl carbon bonded to C_{carb}	0.000	3.6170	0.619
C_{phenyl}	phenyl carbon bonded to H	−0.100	3.6170	0.619
c3	methyl carbon	−0.300	3.8754	0.163
c2	sp^3 carbon bonded to 2 H atoms (ethanol)	−0.170	3.8754	0.163
c2	sp^3 carbon bonded to 2 H atoms (CH_2Cl_2)	0.252	3.8754	0.163
c2	sp^3 carbon bonded to 2 H atoms (C_6H_{12})	−0.200	3.8754	0.163
c1	sp^3 carbon bonded to 1 H atom ($CHCl_3$)	0.578	3.8754	0.163
c	sp^3 carbon bonded to 0 H atoms (CCl_4)	0.904	3.4745	0.669
oh	hydroxyl oxygen	−0.380	3.1655	0.650
cl	chlorine	−0.226	3.5349	0.289
ho	hydrogen bonded to O	0.350	0.0000	0.000
h	hydrogen bonded to C	0.100	2.4500	0.159

[a] Capitalized atom types refer to IRMOF-1 atoms, while lower case atom types refer to CVFF atom types.

Table 2. Intramolecular Force Field Parameters for IRMOF-1 and Guests.

Bond Stretching: $E_{bond} = k_1(r - r_0)^2$.

bond	k_1 (kJ·mol^{-1}·Å^{-2})	r_0 (Å)
C_{phenyl}–C_{phenyl}	2008.3	1.34
C_{phenyl}–h	1520.5	1.08
C_{phenyl}–C_{carb}	1469.6	1.40
C_{carb}–O_{carb}	2259.4	1.25
c3–c2	1350.2	1.526
h–c3	1425.1	1.105
c2–oh	1606.7	1.420
h–c2	1425.1	1.105
oh–ho	2317.7	1.000

Angle Bending: $E_{angle} = k_2(\theta - \theta_0)^2$.

angle	k_2 (kJ·mol^{-1}·rad^{-2})	θ (°)
C_{phenyl}–C_{phenyl}–C_{phenyl}	376.6	120.0
C_{phenyl}–C_{phenyl}–h	154.8	120.0
C_{phenyl}–C_{phenyl}–C_{carb}	145.1	120.0
C_{phenyl}–C_{carb}–O_{carb}	228.0	113.0
O_{carb}–C_{carb}–O_{carb}	606.7	135.0
h–c3–c2	185.8	110.0
h–c3–h	165.3	106.4
c3–c2–oh	292.9	109.5
h–c2–c3	185.8	110.0
h–c2–oh	238.5	109.5
h–c2–h	165.3	106.4
c2–oh–ho	244.8	106.0
c2-c2-c2	195.0	110.5
c2-c2-h	185.8	110.0
h-c2-h	165.3	106.4

Table 2. (cont'd)

Dihedral Angle: $E_{\text{dihedral}} = k_3[1 + d\cos(n\phi)]$.

angle	k_3 (kJ·mol^{-1})	d	n
C_{phenyl}-C_{phenyl}-C_{phenyl}-C_{phenyl}	12.5520	–1	2
C_{phenyl}-C_{phenyl}-C_{phenyl}-C_{carb}	12.5520	–1	2
C_{phenyl}-C_{phenyl}-C_{phenyl}-h	12.5520	–1	2
C_{carb}-C_{phenyl}-C_{phenyl}-h	12.5520	–1	2
h-C_{phenyl}-C_{phenyl}-h	12.5520	–1	2
C_{phenyl}-C_{phenyl}-C_{carb}-O_{carb}	10.4900	–1	2
h-c3-c2-oh	0.6615	1	3
h-c3-c2-h	0.6615	1	3
c3-c2-oh-ho	0.5439	1	3
h-c2-oh-ho	0.5439	1	3
c2-c2-c2-c2	0.6615	1	3
c2-c2-c2-h	0.6615	1	3
h-c2-c2-h	0.6615	1	3

Improper Torsion: $E_{\text{improper}} = k_4[1 + d\cos(n\phi)]$.

angle	k_4 (kJ·mol^{-1})	d	n
C_{phenyl}-C_{phenyl}-C_{phenyl}-h	1.55	–1	2
C_{phenyl}-C_{phenyl}-C_{phenyl}-C_{carb}	41.84	–1	2
C_{phenyl}-C_{carb}-O_{carb}-O_{carb}	41.84	–1	2

All molecular dynamics simulations were performed with the LAMMPS code.[41] Short-range (real space cutoff 10.0 Å) and bonded energy terms were calculated every 0. 5 fs, and long-range electrostatic terms were evaluated every 1.0 fs using an efficient particle-particle particle-mesh solver.[42] The initial atomic coordinates for pure IRMOF-1 were taken from crystallographic coordinates, which has a cubic unit cell (*Fm–3m* space group) with a lattice parameter of 25.67 Å.[43] A supercell consisting of eight unit cells in a 2 x 2 x 2 grid was then prepared, resulting in 3392 atoms with a supercell lattice parameter of 51.34 Å. For pure IRMOF-1, a set of constant-volume (0.1 ps thermostat relaxation time) and constant-pressure (0.0 atm, 1.5 ps barostat relaxation time) simulations were performed at 300 K to equilibrate the system. Thermal expansion data were obtained from a series of *NPT* (number of particles, pressure, temperature) simulations between 200 – 1000 K. At each temperature, a 250-ps pre-equilibrium stage was followed by a 1000-ps production stage. Symmetry constraints were removed during the *NPT* simulations, and each lattice parameter was varied independently (anisotropic volume changes). In all cases, the average lattice parameters in *x*, *y*, and *z* for a given system were within statistical error. For the vibrational analysis, a 40-ps *NVE* (number of particles, volume, potential energy) simulation was performed on an equilibrated configuration from the 300 K *NPT* stage. Atomic velocities were collected every 4 fs, and a Fourier transform of the velocity autocorrelation function produces a power spectrum. A windowing gap of 1500 frames (6 ps) was used to give a spectrum resolution of approximately 2.78 cm^{-1}. Energy-volume and pressure-volume results were obtained from a series of 1000-ps *NVT* (number of particles, volume, temperature) simulations at 300 K. Results for average pressure and potential energy were obtained as the (isotropic) lattice parameter was increased from 25.35 Å to 26.0 Å. Instantaneous pressures were calculated from the virial theorem,[44] and a final pressure was obtained by block averaging.

Unlike the *NPT* simulations in which no symmetry constraints were applied, cubic symmetry was imposed on the *NVT* simulations used to calculate the bulk modulus. In a separate set of *NVT* simulations used to calculate the Young's modulus, one lattice parameter was gradually incremented while the other lattice parameters were kept at their equilibrium values. The elastic moduli were also calculated via energy minimization with initial atomic coordinates taken form the crystal structure of IRMOF-1.[43] These calculations correspond to 0 K state and provide a basis for comparison with DFT results.

For guest adsorption simulations, the choice of guests (listed in Table 3) and loadings were taken from gravimetric data, representing fully saturated IRMOF-1 pores under ambient pressure and a temperature of 295 K.[43] The guest molecules were inserted into the pores in a grid pattern so that close contacts between guest and the framework were avoided. The guest molecules were then subjected to *NVT* annealing (300 K – 1000 K followed by 1000 K – 300 K) while keeping the framework atoms fixed. Average lattice parameters were obtained from a 1000-ps production simulation (*NPT* ensemble at 300 K) as discussed above. An *NVT* simulation of each guest in the pure liquid phase was performed at 300 K after *NVT* annealing as described above. In each case, the supercell contained 1000 molecules, and the volume corresponded to the bulk liquid density. The diffusion of benzene within IRMOF-1 pores was studied from 500-ps *NVE* simulations. Each unit cell contained 10 benzene molecules, corresponding to approximately 11 % by mass.[45] Atomic coordinates were stored every 1.0 ps, and benzene self-diffusion coefficients were obtained from the slope of the mean-square-displacement vs. time plot.[46]

3.3   Results

3.3.1 Structural Validation and Mechanical Properties

MD simulations show that our non-bonded force field accurately predicts the IRMOF-1 structure as a function of temperature, in addition to achieving the observed room-temperature unit-cell dimensions. In particular, the unusual feature of negative thermal expansion is accurately reproduced (Fig. 5). As temperature is increased above 200 K, the simulated lattice parameter decreases. A linear regression indicates that the lattice parameter would be 25.74 Å at 0 K, in agreement with the DFT result of 26.09 Å.[47] Although the simulated lattice parameters are slightly lower (~ 0.2 Å) than the experimental values for evacuated IRMOF-1, the trend of negative thermal expansion is in good agreement with both experiment and other simulations.[21] Using linear regression to calculate lattice parameter values at 30 K and 293 K, we find an increase in unit cell volume of 1.0 %, in exact agreement with XRD results that show the same percentage increase in unit cell volume ($\approx$ 200 Å^3 or 0.1 Å in lattice parameter) over the same temperature range.[48] Dubbeldam *et al*.[21] also reported similar agreement with experiment using their flexible force field. They also derived thermal-expansion coefficients from their simulations, concluding that IRMOFs outperform other contracting materials.
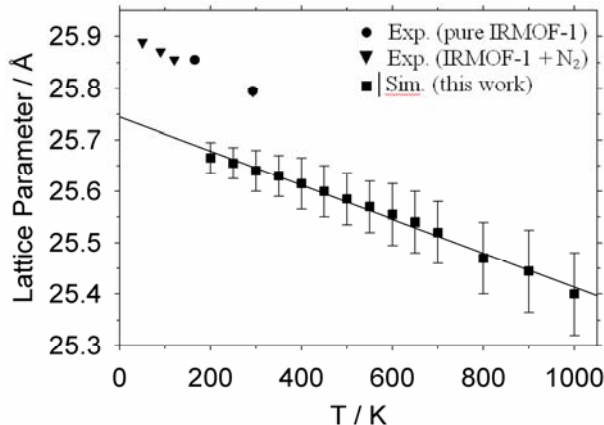
Figure 5. Temperature dependence of the simulated lattice parameter compared with experimental data.[48,49] Error bars indicate uncertainties in the simulated lattice parameters. The solid line represents a linear regression through the simulation results.

Predicted pressure-volume and energy-volume relationships are in good agreement with first-principles calculations. These dependencies were examined by performing constant-volume MD simulations at 300 K, and force field energy minimizations which, like the DFT calculations, correspond to 0 K . In Figure 6 we show that the minimum in potential energy at 300 K is achieved when the lattice parameter is between 25.70 Å − 25.75 Å, but this value increases to 26.05 Å using energy minimization (0 K). These lattice parameters fall within the range of energy-minimized DFT values (25.58 Å – 26.04 Å)[50] so both calculated lattice parameters agree with experimental XRD values.[9,43] The effect of negative thermal expansion is apparent in Figure 2, and also noteworthy is the effect of thermal motion on the curvature at 300 K. This suggests a change in mechanical properties between 0 K and 300 K, which we explore below. The *PV* relationships predicted by our force field are compared with DFT results[50] in Figure 7. At 300 K, the lattice parameter (and volume) vary linearly with pressure over the range 25.6 Å – 26.0 Å. Further reductions in lattice parameter below 25.4 Å do not result in a continued increase in pressure, although the DFT and energy minimization results are linear at positive and negative pressures. At these reduced volumes, the MD simulations predict a disordered structure and eventual collapse of the framework. To our knowledge, the stability of IRMOF-1 at these high pressures has not been investigated experimentally. The calculated slope (-1.30 Å·GPa^{-1}) is nearly triple the value obtained from DFT calculations (-0.46 Å·GPa^{-1})[50] or the force field energy minimizations (-0.43 Å·GPa^{-1}). We have already seen that temperature effects control the structure of IRMOF-1, but they seem to play an important role in the mechanical properties as well.
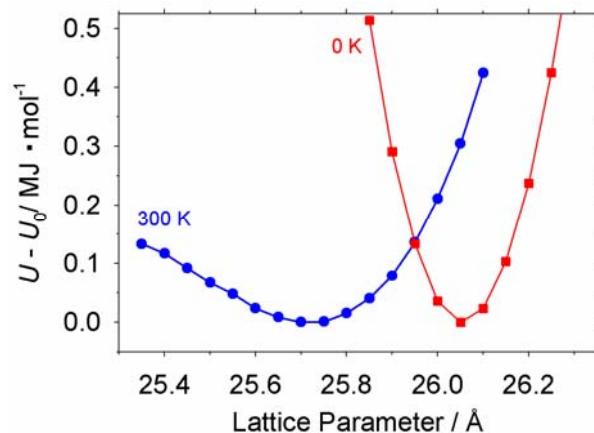
Figure 6. Average potential energy (U) relative to the equilibrium potential energy (U_0) versus lattice parameter from a series of *NVT* simulations at 300 K and energy minimizations (0 K).
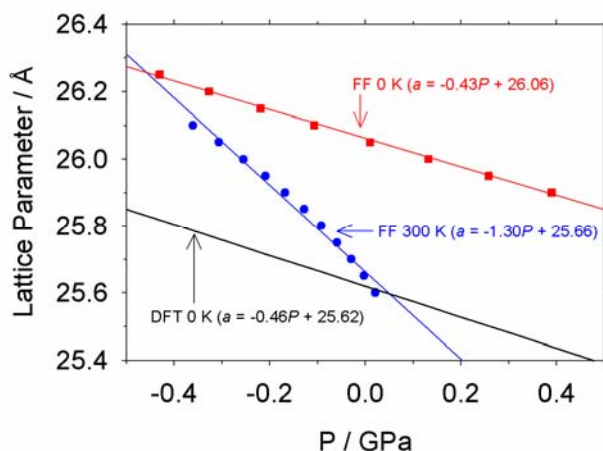
Figure 7. Pressure dependence of IRMOF-1 at 0 K and 300 K. Force field (FF) simulations from this work were calculated from a series of *NVT* simulations (300 K) and energy minimizations (0 K). Pressures were obtained from ensemble averages (300 K) and energy-minimization (0 K). Colored lines represent linear regressions of the FF simulation data, and the black line represents the linear regression from DFT calculations.[50]

We calculated the bulk modulus (B_0) from the force field simulations by fitting energy-volume results to an equation of state.[51] The corresponding figures are shown as Supporting Information, and the results are given in Table 3. The force field result at 0 K is in good agreement with the corresponding DFT result, which suggests that our nonbonded approach for modeling of IRMOF-1 accurately captures the structural and mechanical properties from the more expensive quantum calculations. However, only the 300 K force field result is in agreement with the room temperature nanoindentation experiment. The force field results at 300 K includes thermal effects and represent an averaged structure, which result in a much lower bulk modulus than the energy-minimization results (0 K).

Table 3. Comparison of force field (FF) calculations of bulk modulus (B_0) and Young's modulus (E_0) with DFT calculations and nanoindentation experiments.

| | Energy Min. (0 K) | | MD Sim. (300 K) | Experiment |
	FF (this work)	DFT[52]	FF (this work)	(room temp)[52]
B_0 (GPa)	20.0	16.3	6.4	8.6
E_0 (GPa)	35.5	21.9	14.9	7.9

DFT methods are usually quite accurate at predicting mechanical properties such as the bulk modulus, but in the case of IRMOF's the large pore volumes may make it difficult to obtain accurate energy-strain relationships. A more direct comparison with the nanoindentation experiments can be made by calculating the Young's modulus, E_0. Starting with the equilibrium (relaxed state), one lattice parameter is increased in small increments, and the potential energy is determined by *NVT* simulation (300 K) or energy minimization (0 K). The Young's modulus can then be determined as follows:[53]

$$\frac{\Delta U}{V_0} = E_0 \left(\frac{1}{2} \varepsilon^2 + \frac{1}{3} A\varepsilon \right) \tag{2}$$

where $\Delta U = U - U_0$ is the difference in potential energy between the loaded (U) and relaxed (U_0) states, $\varepsilon = (l-l_0)/l$ is the load strain determined from the relaxed (l) and strained (l_0) lattice parameter, and A is a fitting parameter. The plot corresponding to eqn 2 is shown in the Supporting Information. Unlike the bulk modulus comparison, the force field overpredicts the Young's modulus 0 K compared with the DFT result (21.9 GPa).[52]. However, at room temperature we obtain E_0 = 14.9 GPa, which is much closer to the experimental value (7.9 GPa)[52] than that obtained by DFT. We can therefore conclude that a nonbonded, flexible force field approach successfully predicts the mechanical properties of IRMOF-1.

3.3.2 Energetic validation

We examined the vibrational motion of IRMOF-1 at 300 K as a stringent validation of the force field. Recently published experimental spectra of IRMOF-1[54-56] and analogous inorganic complexes provide a basis for comparison[57,58] In addition, there are two recently published spectra obtained from force field simulations.[33,34] Unlike our nonbonded approach, however, these force fields include bonded terms between all atoms, including Zn, O_{cent}, and O_{carb}.

We concentrate on the Zn-O interactions (200 cm^{-1} – 1000 cm^{-1}) as these are controlled only by nonbonded interactions. Vibrations associated with the BDC phenyl ring are primarily governed by the bond-stretch and angle-bend portions of the CVFF force field, which are used essentially unaltered in our force field. To obtain vibrational information from MD simulations we computed power spectra for Zn, O_{cent}, O_{carb}, and C_{carb} atoms, as shown in Figure 8 (top); frequencies are compared with computational and experimental results in Table 4. Peaks determined from a normal mode analysis[33,47] can usually be associated with specific vibrational modes, such as a symmetric Zn-O_{cent} stretch. This is not possible with power spectra, but vibrational modes can be tentatively assigned by examining the contributions from specific atom types.

Spectroscopic peaks between 530 cm^{-1} and 560 cm^{-1} are typically used to identify ZnO_4 vibrations,[57,58] and for IRMOF-1 the 534 cm^{-1} band in the infrared spectrum has been assigned to

the Zn-O stretching vibration.[56] Our power spectra exhibit peaks in this region at 500 cm^{-1}, 550 cm^{-1}, and 575 cm^{-1} that involve Zn, O_{cent}, and O_{carb} atoms. Additional Zn- O_{cent} modes are found between 185 cm^{-1} and 280 cm^{-1}, in agreement with bonded force field methods.[33] Similar modes are observed experimentally near 340 cm^{-1} for a Zn-acetate complex.[57] At higher frequencies, several peaks are seen for O_{carb} and C_{carb} between 720 cm^{-1} and 815 cm^{-1} that involve Zn and O_{cent} atoms, but to a much smaller extent. These modes likely correspond to carboxylate bending, with minor involvement of the inorganic Zn and O_{cent} atoms. Infrared and Raman peaks in this region have been assigned to O-C-O scissoring motions and other modes.[59,60] We take this agreement to be strong confirming evidence that the non-bonded approach captures essential aspects of the forces governing MOF structure.
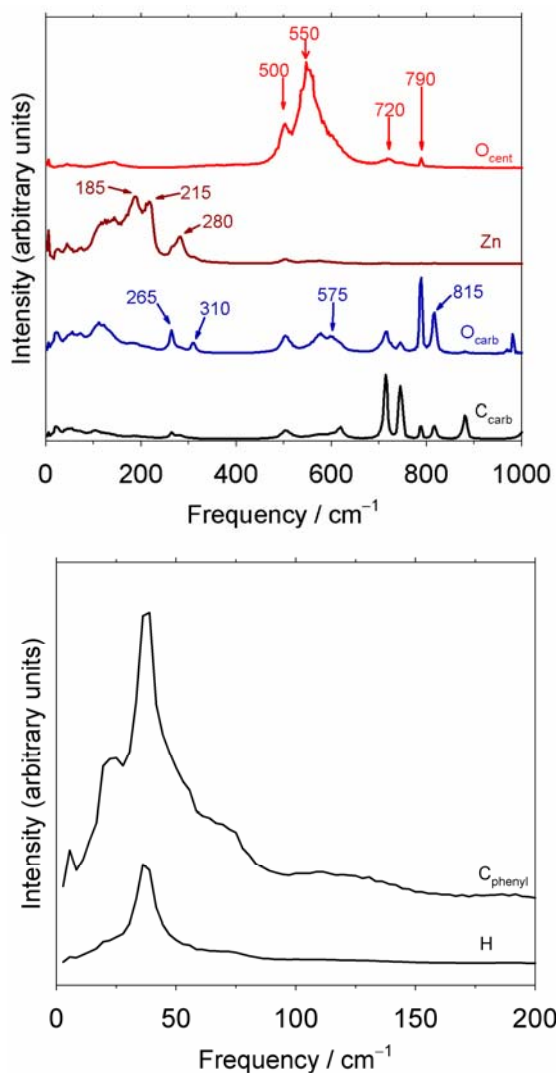
Figure 8. IRMOF-1 atomic power spectra for atom types Zn, O_{cent}, and carboxylate atoms (top), and for H and C_{phenyl} showing the internal rotation of the C_6H_4 unit (bottom).

Table 4. Comparison of calculated vibrational frequencies (in cm^{-1}) for IRMOF-1.

Mode	This Work	Bonded FF[33]	Bonded FF[34]	DFT[47]	Exp.[38,56]
C_6H_4 torsion	40		40		
$Zn-O_{cent}$ symmetric	185, 215, 280	200, 213		136	
$Zn-O_{cent,}$ asymmetric	510, 550-560	516-530	664	512	534
$Zn-O_{carb}$	500, 575-600	572, 576	552	579, 606	
Carboxylate	720, 790, 815		759, 972	749, 830	750, 825

In addition to these vibrations, a strong band near 40 cm^{-1} is seen (Figure 8) that involves phenyl C and H atoms. We assign this band to the internal (torsional) rotation of the phenyl ring. This result agrees with a DFT/B3LYP normal mode analysis, in which the frequency of this motion was predicted to occur between 60 cm^{-1} and 80 cm^{-1}.[33] The temperature dependence of atomic motion within the framework predicted by the MD simulations is also consistent with recent NMR studies, which detected the torsional "flips" of aromatic rings in IRMOF-1.[61] At 300 K, almost no such motion is seen, but at 400 K almost all phenyl rings exhibit this behavior. Although we did not quantify the torsional behavior by extracting an activation barrier, our simulations exhibit similar phenomena, as shown in an animation of MD results provided in the Supporting Information. Another DFT calculation suggested that an energy barrier of approximately 51.8 kJ·mol^{-1} exists for the 90° rotation of the linker,[50] Recent quasielastic neutron scattering measurements of IRMOF-1 at 4 K showed no evidence of any free rotation of the BDC linker,[50] in agreement with the low-temperature deuterium NMR data.[61] However, above room temperature, deuterium NMR shows evidence of phenyl rings undergoing 180° flips.[61] At 223 K and 298 K, the NMR signal represents a superposition of mostly static and a small fraction of "flipping" phenyl rings. At 373 K, however, all phenyl rings appear to undergo the flipping motion. Our simulation results at 300 K and 400 K are consistent with the NMR results. At lower temperatures, the fraction of phenyl rings undergoing this motion appears to be related to the synthetic method. The fast precipitation method characteristic of the low-surface-area phase (MOCP-L) is thought to contain impurities that result in increased C_6H_4 torsional motion compared with IRMOF-1.[61]

3.3.3 Structural changes with adsorbed species
As discussed in the Introduction, the dimensions of MOF unit cells can change significantly upon adsorption of guest molecules. Using our flexible force field, MD simulations can be used to quantify any changes in unit cell structure and free volume upon adsorption, and agreement with experimental measurements of such changes constitutes a further validation of force field performance. Gravimetric data for hydrocarbons and chloromethanes adsorbed within IRMOF-1 are available for comparison with our MD simulations (Table 5).[43] As a starting point for MD simulations, we used the number of adsorbate molecules contained in completely filled IRMOF-1 pores obtained from the liquid sorption data given in ref 43. Values for free volume and the fraction of the pore volume occupied by guests were computed directly from the average lattice parameters (*NPT* simulations at 300 K, standard deviations less than 0.03 Å), while the Dubinin-Raduskhvich equation was used to estimate these values from the gravimetric data.[43] Unfortunately, experimental lattice parameters were not reported for the adsorbed hydrocarbon and chloromethane systems. In addition to the hydrophobic guests commonly used in IRMOF-1 adsorption experiments, we also include ethanol, since it is a hydrophilic guest capable of forming hydrogen bonds between guests and the framework.

As seen in Table 5, in all cases the guest molecules occupy approximately 53.5 – 56.0 % of the total volume, in good agreement with experiment.[43] There are five pores within the IRMOF-1 unit cell, so the predicted pore occupancy ranges from 10 molecules in the case of hexane to 19 molecules in the case of ethanol. Interatomic distances computed from radial distribution functions (Table 6) indicate that, with the exception of hexane, guest molecules appear to be somewhat more tightly packed in the bulk liquid than in the IRMOF-1 pores. To make this comparison, we simulated the bulk liquids in the *NVT* ensemble, using their experimental density at 1.0 atm and 300 K. The results indicate that C-C distances are approximately 3% greater in the IRMOF-1 pore than in the bulk for the chlorinated species and ethanol, while the distances are unchanged for hexane. Cl-Cl distances are also larger in the MOF than in the bulk for the polar compounds CH_2Cl_2 and $CHCl_3$, but are unchanged in the case of non-polar CCl_4. O-O distances in ethanol are also essentially unchanged from the bulk liquid. We conclude that the local guest structure within the pores is essentially identical to the bulk phase for these compounds.

These results concerning the local guest structure are consistent with the predicted changes in unit cell dimensions upon adsorption, which are small. In the case of the chlorinated species and hexane, a slight increase in cell volume is predicted (0.7 – 1.5%). In contrast, ethanol, which is both more polar and capable of hydrogen bonding with O_{carb} atoms of IRMOF-1, there is a small contraction (–0.9 %). This result is consistent with our previous simulations of water adsorption in IRMOF-1.[35]

Benzene is omitted from Tables 5 and 6 because MD simulations involving this molecule (63 C_6H_6 per unit cell) result in a severely distorted framework. Given that our results for other guests agree with experiment, simulations of IRMOF-1 pores completely filled with benzene may require an adjustment of the MOF-C_6H_6 force field parameters. Noting that a modified version of our force field greatly reduces the attractive potential of the O_{carb} atom,[21] it is possible that such an approach would yield better results for benzene adsorption.

Table 5. Simulation Results for Guest Adsorption.

				Simulation			Experiment[43]	
Guest	guest/ unit cell	guest mass %	lattice parameter (Å)	free volume $(cm^3{\cdot}g^{-1})^a$	guest volume $\%^b$	free volume $(cm^3{\cdot}g^{-1})^a$	guest volume $\%^b$
None			25.64				
CH_3CH_2OH	95	41.5	25.56	0.90	55.2		
CH_2Cl_2	88	54.8	25.70	0.91	55.1	0.93	55
$CHCl_3$	71	57.9	25.69	0.93	56.0	0.94	55
CCl_4	59	59.6	25.70	0.92	55.7	0.94	55
C_6H_{12}	51	41.1	25.77	0.90	53.5	0.92	54

[a] Calculated as the volume of guest (assuming bulk liquid density) divided by the unit cell mass of pure IRMOF-1.

[b] Calculated as the ratio of guest volume (assuming bulk liquid density) to total volume.

Table 6. Intermolecular Distances for Guest Molecules from Radial Distribution Functions.

Guest	C-C		Cl-Cl		O-O	
	IRMOF-1	Bulk	IRMOF-1	Bulk	IRMOF-1	Bulk
CH_3CH_2OH	4.65	4.53			3.03	3.02
CH_2Cl_2	5.13	5.00	3.95	3.79		
$CHCl_3$	5.38	5.22	3.83	3.68		
CCl_4	5.82	5.63	3.68	3.69		
C_6H_{12}	2.99	2.98				

3.3.4 Benzene diffusion at low loading

As a final test of our force field approach, we compared simulated self-diffusion coefficients (D_{self}) for adsorbed benzene with both the flexible force field of Tafipolsky *et al.*[24] and experimental NMR results.[45] A series of *NVT* simulations were performed at temperatures of 250 K, 300 K, 350 K, and 400 K, using a low benzene loading of 10 molecules / unit cell (11 wt %) to match the experimental system. Results are displayed in Figure 9 as Arrhenius plots. Three experimental values of D_{self} were reported. The upper and lower blue points in Fig. 9 represent short-time "intracrystalline" diffusion coefficients (3.8 x 10^{-10} $m^2 \cdot s^{-1}$ and 1.9 x 10^{-9} $m^2 \cdot s^{-1}$, average of two reported values in each case), while the middle blue point represents the arithmetic mean of these two values for D_{self} (1.4 x 10^{-9} $m^2 \cdot s^{-1}$).[45] For purposes of comparison with our results, the intracrystalline value is the most appropriate one.

The D_{self} determined from the MD simulation differs from the experimental value by a factor of about 8. However, the computed activation energy for diffusion of 14.3 kJ·mol^{-1} is in excellent agreement with the value of 14.0 kJ·mol^{-1} predicted by Amirjalayer *et al* (black line) using the MM3-based flexible force field.[24] Keeping the framework atoms fixed at their crystallographic coordinates[43] results in lower values of D_{self} (green line) and a significantly lower activation energy of 9.8 kJ·mol^{-1}, highlighting the importance of a flexible force field when modeling transport of larger hydrocarbon guests. A similar effect is seen in simulations of methane diffusion in zeolites, but is less prominent for larger alkane guests.[62] At the higher guest loadings in those simulations, guest-guest interactions are expected to dominate diffusional motion, so the effect of framework flexibility should be reduced.[62]

The difference in benzene D_{self} values between the two flexible force field simulations, combined with the difficulty in simulating a system with much higher benzene loading (see above) indicate that the general-purpose CVFF force field parameters for organic guest molecules are not sufficient for MOF-(aromatic guest) simulations. Rather, guest parameters that produce good bulk properties should be considered for simulations at high loading. It should also be noted that the benzene D_{self} values from another CVFF-based flexible force field[21] are also in good agreement with the MM3-based results, which suggests again that the nonbonded parameters for MOF atoms, particularly O_{carb} atoms, need to be re-parameterized from the CVFF or metal oxide values.
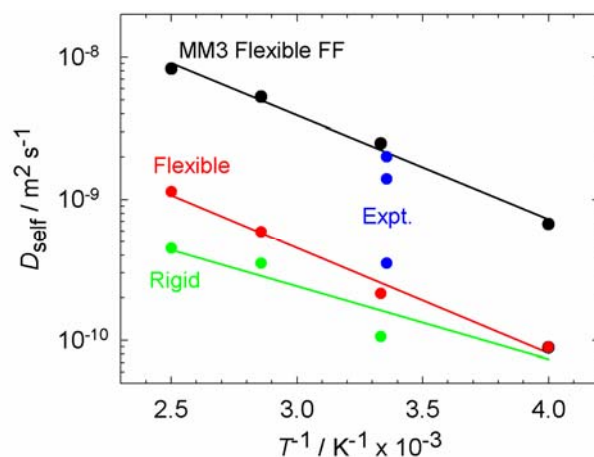
Figure 9. Comparison of benzene diffusion coefficients from simulations and experiment. Red and green circles are simulation results from this work for flexible and rigid frameworks, respectively. Black circles are simulation results from a flexible MM3-based forcefield.[24] Blue circles are experimental data points for intracrystalline diffusion coefficients (upper and lower points) and effective diffusion coefficient (middle).[45] Solid lines represent linear regressions from each simulation data set.

3.4   Conclusions

We report an extensive series of MD simulations designed to validate the flexible force field for IRMOF-1 we originally developed to model the interaction of water with this framework. Our non-bonded approach is computationally inexpensive, but it produces structural and energetic results that are in excellent agreement with experimental results, as well as more expensive (first principles) computational methods. For evacuated IRMOF-1, the unusual property of negative thermal expansion is predicted between 200 K and 1000 K, in agreement with both experiment[48] and other force field simulations.[21] Additionally, energy-volume and pressure-volume relationships are in good agreement with DFT results[52] at 0 K and with experimental results at room temperature.[52] The temperature effects of IRMOF-1 mechanical properties has not previously been considered, but our results suggest that the effect of temperature may be dramatic. Overall, we conclude that it is important to include only nonbonded (electrostatic and van der Waals) interactions between Zn and O atoms for simulations of zinc-based MOFs in which the unit cell volume varies (*i.e.*, constant pressure simulations). When Zn-O bonded interactions are included, as they are in other flexible force fields,[33,34] the ability of the framework to undergo volume changes due to chemical or physical changes is severely impaired by bond and angle constraints. A fully bonded model may be suitable for constant-volume simulations to study diffusion or other properties, or when only small changes in the unit cell volume are expected, as might be the case with weakly interacting gases such as hydrogen. In the case of constant-pressure simulations, however, realistic volumes cannot be expected from such a constrained model system.

Our nonbonded parameters for Zn-O interactions in IRMOF-1 were further validated by comparing simulated power spectra with both computational and experimental results. As expected, frequencies for the BDC linker modes agree with experiment, but those intramolecular

interactions are controlled by bond stretch, angle bend, torsional, and improper force field parameters provided by the CVFF portion of our force field. More importantly, our simulated Zn-O frequencies in the region 500 – 575 cm^{-1} lie within the range of frequencies attributed to ZnO$_4$ tetrahedral modes in IRMOF-1[56] and related compounds.[57,58] Our use of simulated power spectra also enables us to detect modes at very low frequencies (< 100 cm^{-1}). Specifically, the predicted torsional frequency of phenyl rings in the BDC linker at 40 cm^{-1} is in agreement with quasielastic neutron scattering results,[50] and the increasing tendency of this motion with increasing temperature is consistent with NMR data.[61] Thus, the accuracy of predicted vibrational data is not sacrificed by omitting bonded terms in the Zn-O component of the force field.

Concerning the adsorption of guest molecules within the IRMOF-1 framework pores, constant-pressure simulations exhibit only slight changes in unit cell volume upon adsorption of guest molecules at high loadings, which is generally in agreement with available crystallographic data. The results shed light on the nature of framework-adsorbate interactions. In particular, we note a trend of slightly decreasing volume when hydrophilic guests such as water or ethanol are adsorbed. This is most likely a consequence of the ability of these molecules to form hydrogen bonds with the framework oxygen atoms. When hydrophobic guests are adsorbed, a slight increase in unit cell volume is seen. At full saturation, guests occupy 53.5 – 56.0% of the unit cell volume, in good agreement with experiment.[43] An examination of guest-guest radial distribution functions shows very little difference in the local structure of guest molecules between the bulk and adsorbed phases, regardless of polarity or hydrogen-bonding ability.

Finally, although our force field reproduces virtually all structural observations reported for IRMOF-1, it underestimates the diffusion constant for benzene and leads to unstable structures at high benzene loadings. The fact that our calculated activation energy is in excellent agreement with a fully bonded force field[24] whose predicted D_{self} for benzene agrees with experiment suggests that the energetics of benzene interaction with the framework are correct, but that the parameters governing benzene-benzene interactions require adjustment. The CVFF parameters for benzene and other guests included in this work were not optimized for the bulk properties of these guests. Since our simulations demonstrate that guest densities approaching liquid values can occur within MOF pores, in future force field development we will optimize our guest parameters to reproduce the densities for bulk liquids.

References

1.   James, S. L. *Chem. Soc. Rev.* **2003**, 32, 276.
2.   Kitagawa, S.; Kitaura, R.; Noro, S. *Angew. Chem. Int. Edit.* **2004**, 43, 2334.
3.   Rowsell, J. L. C.; Yaghi, O. M. *Micropor. Mesopor. Mater.* **2004**, 73, 3.
4.   Férey, G.; Mellot-Draznieks, C.; Serre, C.; Millange, F.; Dutour, J.; Surble, S.; Margiolak, I. *Science* **2005**, 3093, 2040.
5.   Surblé, S.; Serre, C.; Mellot-Draznieks, C.; Millange, F.; Férey, G. *Chem. Comm.* **2006**, 284.
6.   Rowsell, J. L. C.; Yaghi, O. M. *Angew. Chem. Int. Edit.* **2005**, 44, 4670.
7.   Dinca, M.; Han, W. S.; Liu, Y.; Dailly, A.; Brown, C. M.; Long, J. R. *Angew. Chem. Int. Edit.* **2007**, 46, 1419.

8.   Forster, P. M.; Eckert, J.; Heiken, B. D.; Parise, J. B.; Yoon, J. W.; Jhung, S. H.; Chang, J. S.; Cheetham, A. K. *J. Am. Chem. Soc.* **2006**, 128, 16846.

9.   Eddaoudi, M.; Kim, J.; Rosi, N.; Vodak, D.; Wachter, J.; O'Keefe, M.; Yaghi, O. M. *Science* **2002**, 295, 469.

10.   Chen, B. L.; Ma, S. Q.; Zapata, F.; Fronczek, F. R.; Lobkovsky, E. B.; Zhou, H. C. *Inorg. Chem.* **2007**, 46, 1233.

11.   Dubbeldam, D.; Snurr, R. Q. *Molec. Sim.* **2007**, 33, 305.

12.   Garberoglio, G.; Skoulidas, A. I.; Johnson, J. K. *J. Phys. Chem. B* **2005**, 109, 13094.

13.   Mueller, T.; Ceder, G. *J. Phys. Chem. B* **2005**, 109, 17974.

14.   Mulder, F. M.; Dingemans, T. J.; Wagemaker, M.; Kearley, G. *J. Chem. Phys.* **2005**, 317, 113.

15.   Sagara, T.; Klassen, J.; Ganz, E. *J. Chem. Phys.* **2004**, 121, 12543.

16.   Skoulidas, A. I.; Sholl, D. S. *J. Phys. Chem. B* **2005**, 109, 15760.

17.   Yang, Q.; Zhong, C. *J. Phys. Chem. B* **2005**, 109, 11862.

18.   Düren, T.; Sarkisov, L.; Yaghi, O. M.; Snurr, R. Q. *Langmuir* **2004**, 20, 2683.

19.   Düren, T.; Snurr, R. Q. *J. Phys. Chem. B* **2004**, 108, 15703.

20.   Wang, S. *En. Fuels* **2007**, 21, 953.

21.   Dubbeldam, D.; Walton, K. S.; Ellis, D. E.; Snurr, R. Q. *Angew. Chem. Int. Edit.* **2007**, 46, 4496.

22.   Ramsahye, N. A.; Maurin, G.; Bourrelly, S.; Llewellyn, P.; Loiseau, T.; Ferey, G. *Phys. Chem. Chem. Phys.* **2007**, 9, 1059.

23.   Jiang, J. W.; Sandler, S. I. *Langmuir* **2006**, 22, 5702.

24.   Amirjalayer, S.; Tafipolsky, M.; Schmid, R. Angew. *Chem. Int. Ed.* **2007**, 46, 463.

25.   Krungleviciute, V.; Lask, K.; Heroux, L.; Migone, A. D.; Lee, J. Y.; Li, J.; Skoulidas, A. *Langmuir* **2007**, 23, 3106.

26.   Skoulidas, A. I. *J. Am. Chem. Soc.* **2004**, 126, 1356.

27.   Rappe, A. K.; Casewit, C. J.; Colwell, K. S.; Goddard, W. A.; Skiff, W. M. *J. Am. Chem. Soc.* **1992**, 114, 10024.

28.   Mayo, S. L.; Olafson, B. D.; Goddard, W. A. *J. Phys. Chem.* **1990**, 94, 8897.

29.   Jorgensen, W. L.; Maxwell, D. S.; Tirado-Rives, J. *J. Am. Chem. Soc.* **1996**, 118, 11225.

30.   Fletcher, A. J.; Thomas, K. M.; Rosseinsky, M. J. *J. Solid State Chem.* 178, 178, 2491.

31.   Uemura, K.; Matsuda, R.; Kitagawa, S. *J. Solid State Chem.* **2005**, 178, 2420.

32.   Cussen, E. J.; Claridge, J. B.; Rosseinsky, M. J.; Kepert, C. J. *J. Am. Chem. Soc.* **2002**, 124, 9574.

33.   Tafipolsky, M.; Amirjalayer, S.; Schmid, R. *J. Comp. Chem.* **2007**, 28, 1169.

34.   Huang, B. L.; McGaughey, A. J. H.; Kaviany, M. *Int. J. Heat Mass Transfer* **2007**, 50, 393.

35.   Greathouse, J. A.; Allendorf, M. D. *J. Am. Chem. Soc.* **2006**, 128, 10678.

36.   Teter, D. M., Unpublished parameters.

37.   Ref 24 states: "Our extended MM3 forcefield correctly predicts the structure of MOF-5…Note that this is in contrast to the very recently published forcefield focusing on a noncovalent description of the Zn-O interaction." Ref. 21 states: "It [i.e., the new force field referenced here as Ref. 21] is similar in spirit to the model of Greathouse and Allendorf, but differs in the treatment of the carboxylate group and has the advantage of being calibrated to experimental data."

38.	Huang, L. M.; Wang, H. T.; Chen, J. X.; Wang, Z. B.; Sun, J. Y.; Zhao, D. Y.; Yan, Y. S. *Microporous Mesoporous Mater.* **2003**, 58, 105.

39.	Kaye, S. S.; Dailly, A.; Yaghi, O. M.; Long, J. R. *J. Am. Chem. Soc.* **2007**, 129, 14176.

40.	Dauber-Osguthorpe, P.; Roberts, V. A.; Osguthorpe, D. J.; Wolff, J.; Genest, M.; Hagler, A. T. *Proteins: Struct., Funct., Genet.* **1988**, 4, 31.

41.	Plimpton, S. J. *J. Comp. Phys.* **1995**, 117, 1.

42.	Plimpton, S. J.; Pollock, R.; Stevens, M. "Particle-Mesh Ewald and rRESPA for parallel molecular dynamics simulations"; Eighth SIAM Conference on Parallel Processing for Scientific Computing, **1997**.

43.	Li, H.; Eddaoudi, M.; O'Keeffe, M.; Yaghi, O. M. *Nature* **1999**, 402, 276.

44.	Wang, J. W.; Kalinichev, A. G.; Kirkpatrick, R. J. *J. Phys. Chem. B* **2005**, 109, 14308.

45.	Stallmach, F.; Groger, S.; Kunzel, V.; Karger, J.; Yaghi, O. M.; Hesse, M.; Muller, U. *Angew. Chem. Int. Edit.* **2006**, 45, 2123.

46.	Allen, M. P.; Tildesley, D. J. *Computer Simulation of Liquids*; Clarendon Press: Oxford, **1987**.

47.	Civalleri, B.; Napoli, F.; Noel, Y.; Roetti, C.; Dovesi, R. *CrystEngComm* **2006**, 8, 364.

48.	Rowsell, J. L. C.; Spencer, E., C.; Eckert, J.; Howard, J. A. K.; Yaghi, O. M. *Science* **2005**, 309, 1350.

49.	Eddaoudi, M.; Moler, D. B.; Li, H.; Chen, B.; Reineke, T. M.; O'Keeffe, M.; Yaghi, O. M. *Acc. Chem. Res.* **2001**, 34, 319.

50.	Zhou, W.; Yildirim, T. *Phys. Rev. B* **2006**, 74.

51.	Valencia, F.; Romero, A. H.; Hernandez, E.; Terrones, M.; Terrones, H. *New J. Phys.* **2003**, 5, 123.

52.	Fung, Y. C.; Tong, P. *Classical and Computational Solid Mechanics*; World Scientific: Singapore, **2001**.

53.	Bahr, D. F.; Reid, J. A.; Mook, W. M.; Bauer, C. A.; Stumpf, R.; Skulan, A. J.; Moody, N. R.; Simmons, B. A.; Shindel, M. M.; Allendorf, M. D. *Phys. Rev. B* **2007**, 76, 184106.

54.	Diao, J.; Gall, K.; Dunn, M. L. *J. Mech. Phys. Solids* **2004**, 52, 1935.

55.	Bordiga, S.; Lamberti, C.; Ricchiardi, G.; Regli, L.; Bonino, F.; Damin, A.; Lillerud, K. P.; Bjorgen, M.; Zecchina, A. *Chem. Comm.* **2004**, 2300.

56.	Bordiga, S.; Vitillo, J. G.; Ricchiardi, G.; Regli, L.; Cocina, D.; Zecchina, A.; Arstad, B.; Bjorgen, M.; Hafizovic, J.; Lillerud, K. P. *J. Phys. Chem. B* **2005**, 109, 18237.

57.	Hermes, S.; Schroder, F.; Amirjalayer, S.; Schmid, R.; Fischer, R. A. *J. Mater. Chem.* **2006**, 16, 2464.

58.	Johnson, M. K.; Powell, D. B.; Cannon, R. D. *Spectrochim. Acta A* **1982**, 38, 125.

59.	Berkesi, O.; Andor, J. A.; Jayasooriya, U. A.; Cannon, R. D. *Spectrochim. Acta A* **1992**, 48, 147.

60.	Green, J. H. S.; Kynaston, W.; Lindsey, A. S. *Spectrochim. Acta* **1961**, 17, 486.

61.	Spinner, E. *J. Chem. Soc. B* **1967**, 874.

62.	Gonzalez, J.; Devi, R. N.; Tunstall, D. P.; Cox, P. A.; Wright, P. A. *Micropor. Mesopor. Mater.* **2005**, 84, 97.

63.	Leroy, F.; Rousseau, B.; Fuchs, A. H. *Phys. Chem. Chem. Phys.* **2004**, 6, 775.

[Blank page following section.]

4. GRAND CANONICAL MONTE CARLO SIMULATIONS OF MOF ANALYTE ADSORPTION

4.1 Introduction

The force field model described in the preceding chapter provides a tool for modeling the uptake of analytes by coordination polymers (CP). The resulting information, which is obtained in the form of isosteric heats of adsorption and adsorption isotherms, provides the basis for designing new CP with adsorption properties tuned to yield efficient and selective uptake of desired species. Below we present results of Grand Canonical Monte Carlo (GCMC) simulations for a set of seven metal-organic frameworks (MOFs). The calculations show that selective uptake of analytes is feasible and that certain compounds, such as the explosive RDX, are adsorbed sufficiently tightly that partial pressures as low as 10 ppb result in significant uptake. Overall, these results are convincing evidence that CP in general and MOFs in particular can serve as efficient and selective recognition chemistries for sensing devices such as microcantilevers.

4.2 Methods

GCMC simulations were performed at 298 K using the Sorption module of Materials Studio (Accelrys, Inc.). The MOFs considered in this study are described in Table 7, along with estimates of their surface areas and free volumes. The corresponding organic linkers are shown in Figure 10. Although more robust methods have been used to estimate free volumes,[1-2] the simple approach used here should be effective when examining trends in adsorption. The analytes are described in Table 8 and represent substituted benzenes, explosives, chemical warfare agents, and polycyclic aromatic hydrocarbons (PAHs).

Table 7. Calculated Surface Areas and Free Volumes Using the Connolly Surface Method[3] (REF-Connolly) With a Probe Radius of 1 Å .

MOF	Formula	lattice parameter (Å)[a]	surface area ($m^2 \cdot g^{-1}$)	% free volume
IRMOF-1	$Zn_4O(O_2C\text{-}C_6H_4\text{-}CO_2)$	25.8	3352	79.1
IRMOF-2	$Zn_4O(O_2C\text{-}C_6H_3Br\text{-}CO_2)$	25.8	2677	77.1
IRMOF-3	$Zn_4O(O_2C\text{-}C_6H_3NH_2\text{-}CO_2)$	25.7	3317	76.9
IRMOF-7	$Zn_4O(O_2C\text{-}C_{10}H_6\text{-}CO_2)$	25.8	3414	73.0
IRMOF-8	$Zn_4O(O_2C\text{-}C_{10}H_6\text{-}CO_2)$	30.1	3541	82.8
HKUST-1	$Cu_3[C_6H_3(CO_2)_3(H_2O)_3]$	26.3	3142	64.2
CrMIL-53lp[c]	$Cr(OH)(O_2C\text{-}C_6H_4\text{-}CO_2)$	6.8 x 16.7 x 13.0	3049	55.4

[a] Experimental lattice parameters taken from the literature.[4-6]
[b] The large pore (lp) form of CrMIL-53 was used.
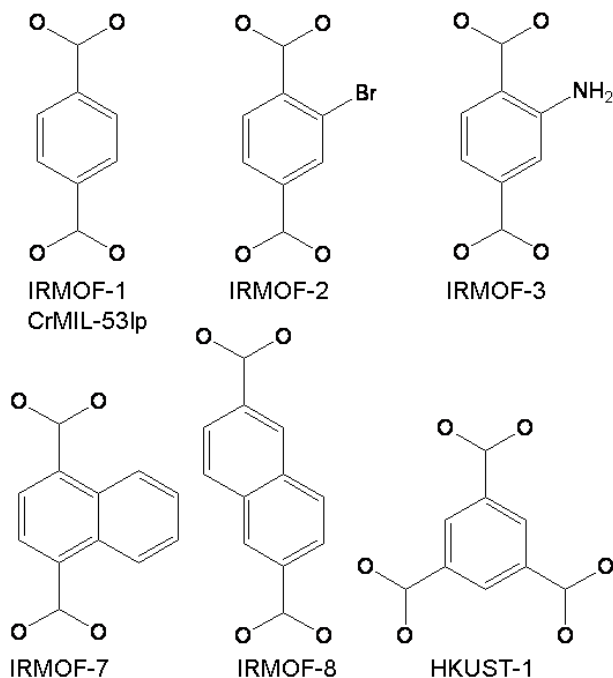
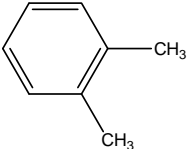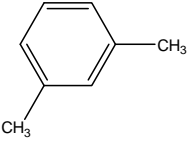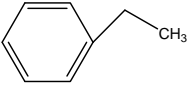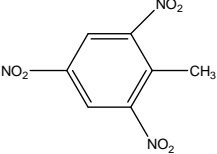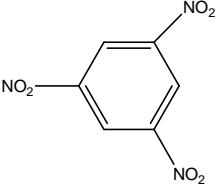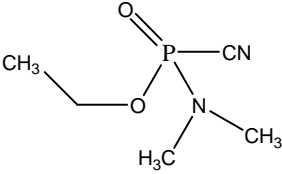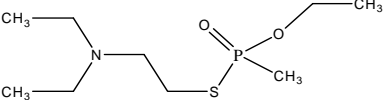**Figure 10.** Linkers for the MOFs considered in this study.

Framework atoms were held at their crystallographic coordinates. For CrMIL-53lp and HKUST-1, structural OH and waters were included, respectively. These oxygen positions were taken from the crystal structures. H atoms were added manually, and their final positions were determined from geometry optimization. Analyte molecules were also treated as rigid bodies, but each inserted molecule was selected from 10 conformations from a previous molecular dynamics simulation. Trial moves included insertion, deletion, conformer exchange, rotation, and translation. For the IRMOFs and HKUST-1, the simulation cell consisted of one unit cell, while a 4 x 2 x 2 supercell was used for CrMIL-53lp. Long-range electrostatics were computed using Ewald summation with an accuracy of 1.0×10^{-4} kcal·mol^{-1}. A cutoff distance of 12 Å was used for short-range interactions.
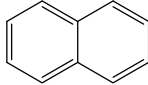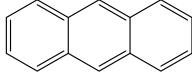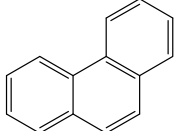
Each simulation consisted of 3×10^5 trial moves, and the last 2.5×10^5 moves were used for averaging. Analyte fugacities ranged from 1.0×10^{-6} kPa to 101 kPa (1 atm). The relatively small number of trial moves is justified given the low analyte fugacities that were considered. As a confirmation, we performed a longer GCMC simulation of o-xylene adsorption by IRMOF-1 at 298 K at a pressure of 101 kPa, with a total of 2×10^6 steps. The average uptake of o-xylene between the shorter and longer simulations was 34 molecules per unit cell and 38 molecules per unit cell, respectively.

Force field parameters were taken from the literature and will only be summarized here. Because frameworks and analytes were treated as rigid bodies, only nonbonded interactions (electrostatics and van der Waals) were included in the simulations. For the IRMOFs, both van der Waals interactions and atomic charges were based on the parameters developed previously for IRMOFs 1, 10, and 16.[7] The van der Waals parameters were based on the Consistent Valence Force Field

(CVFF)[8] and adjusted to fit experimental lattice parameters and adsorption isotherms. Atomic charges were determined from ab initio calculations. Parameters for IRMOF-1, 7, and 8 were used as published.[7] Although IRMOFs 7 and 8 were not included in the original parameterization, their linkers contain similar atom types as IRMOFs 1, 10, and 16. van der Waals parameters for the Br and NH_2 functional groups in IRMOFs 2 and 3 were taken from CVFF without modification. Atomic charges for IRMOFs 2 and 3 were obtained from the same type of ab initio calculations used for IRMOFs 1, 10, and 16.[7] Parameters for HKUST-1 and CrMIL-53lp were taken directly from the literature.[9-10] The van der Waals parameters reported for HKUST-1 depended on the type of analyte,[9] so the values for H_2 were used. That model did not include structural water, so parameters from the Simple Point Charge (SPC)[11] model were used. The flexible model for CrMIL-53lp includes atomic polarization which was not included here.

Table 8. Formula, Abbreviation, and Structure of Analytes.

o-xylene	OX	
m-xylene	MX	
p-xylene	PX	
ethyl benzene	EB	
1,3,5-trinitrotoluene	TNT	
1,3,5-trinitro-1,3,5-triazacyclohexane	RDX	
ethyl dimethylamino-cyanophosphonate	GA	
O-ethyl-S-[2-(diethylamino)ethyl] methylphosphonothioate	VM	

naphthalene	NA	
anthracene	ANTH	
phenanthrene	PHEN	

4.3   Results

Analyte loading at 1 atm pressure is shown in Figure 11 as a function of gravimetric (mg·g^{-1}) and volumetric (molecules·nm^{-3}) uptake. IRMOF-8 shows a much higher gravimetric uptake than the other MOFs, based on its much larger free volume. Surprisingly, CrMIL53-lp shows one of lowest gravimetric and volumetric uptakes even though its free volume is similar to IRMOFs 2 and 3. Free volume effects are normalized in Figure 11b, showing similar volumetric loadings for the Zn-IRMOFs. HKUST-1 and CrMIL53-lp are still underperformers over the range of analytes studied.
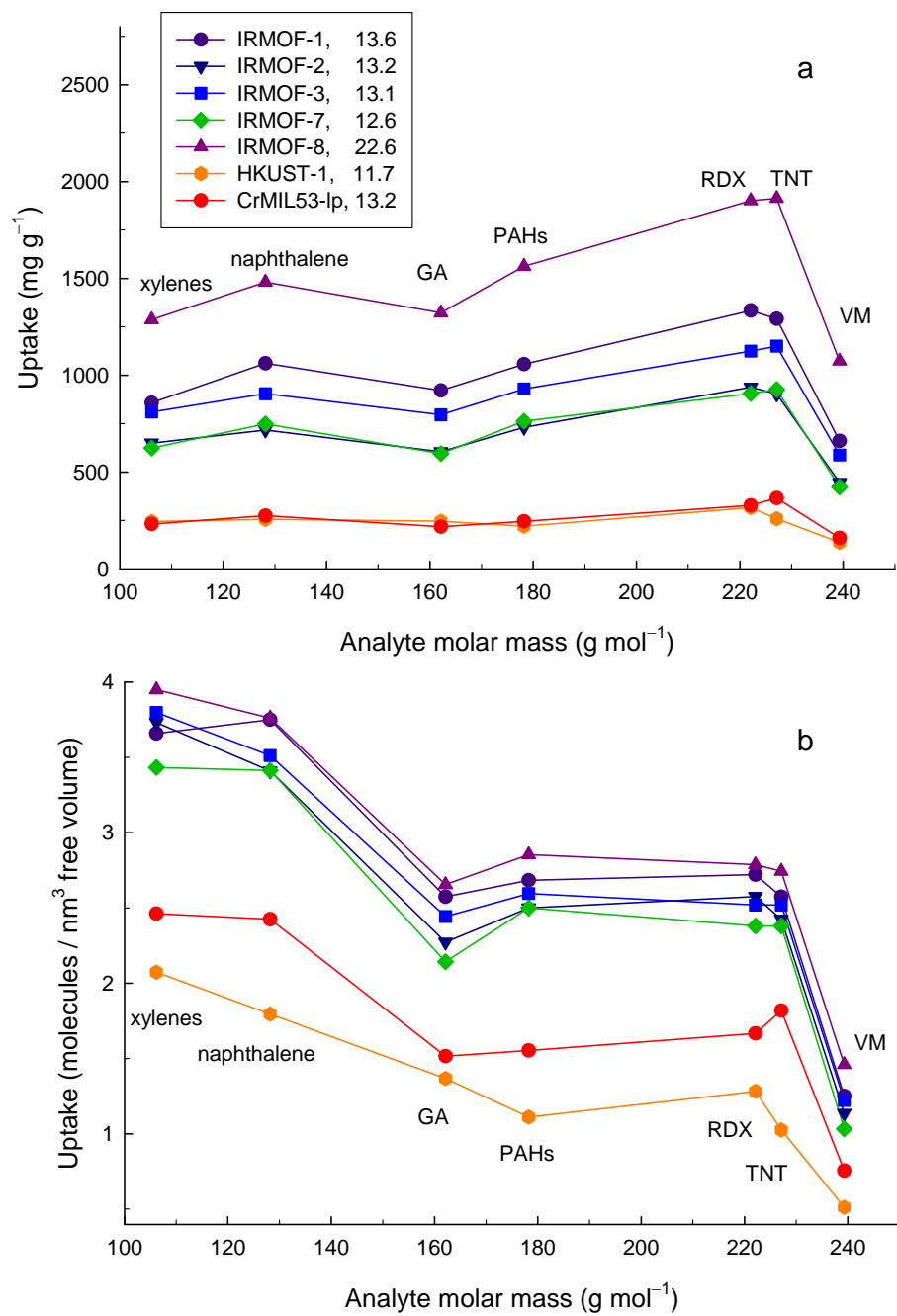
Figure 11. Uptake as a function of analyte molar mass for all MOFs at 1 atm pressure. Uptake is given in both gravimetric (a) and volumetric (b) units. Each MOF is identified in the legend with its corresponding free volume (nm^3) based on the simulation cell. Labels indicate each analyte type, and PAHs refers to polycyclic aromatic hydrocarbons (anthracene and phenanthrene).

A comparison of analyte adsorption energies allows us to predict trends in analyte detection at low concentration. Figure 12 compares the isosteric heats of adsorption from all of the simulations. Several trends are evident. For all analyte types except RDX, CrMIL53-lp shows the highest values of Q_{st}, and HKUST-1 shows the lowest values. Based on these results, it appears that CrMIL53 shows the most promise for low-concentration analyte detection. Within the Zn-IRMOF series, there is little change in Q_{st} for each analyte. The heat of adsorption appears to depend more strongly on the type of metal in a MOF rather than the type of linker. Without experimental confirmation, however, these trends could be dependent on the force field parameters used for each MOF. For each analyte type, the trend in Q_{st} values matches the trend in metal atomic charges for these MOFs ($q_{Cu} < q_{Zn} < q_{Cr}$).
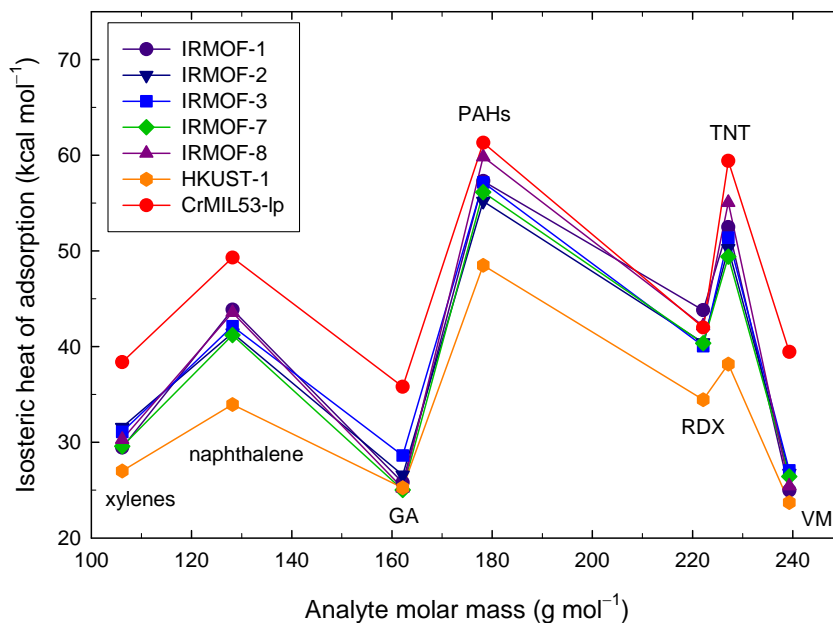
Figure 12. Isosteric heats of adsorption values plotted as a function of analyte molar mass and MOF. Labels indicate each analyte type, and PAHs refers to polycyclic aromatic hydrocarbons (anthracene and phenanthrene).

The onset of adsorption is related to the isosteric heat of adsorption. RDX and naphthalene both adsorb at lower pressures, and each has Qst = 44 kcal/mol. For example, adsorption isotherms for three analytes are shown in Fig. 13. The onset of adsorption for ethyl benzene occurs at a higher pressure since it has a lower Qst of 29 kcal mol^{-1}. Note that the rather high Qst of RDX causes an onset of adsorption at 10^{-6} kPa, equivalent to a partial pressure of 10 ppb at 1 atm.
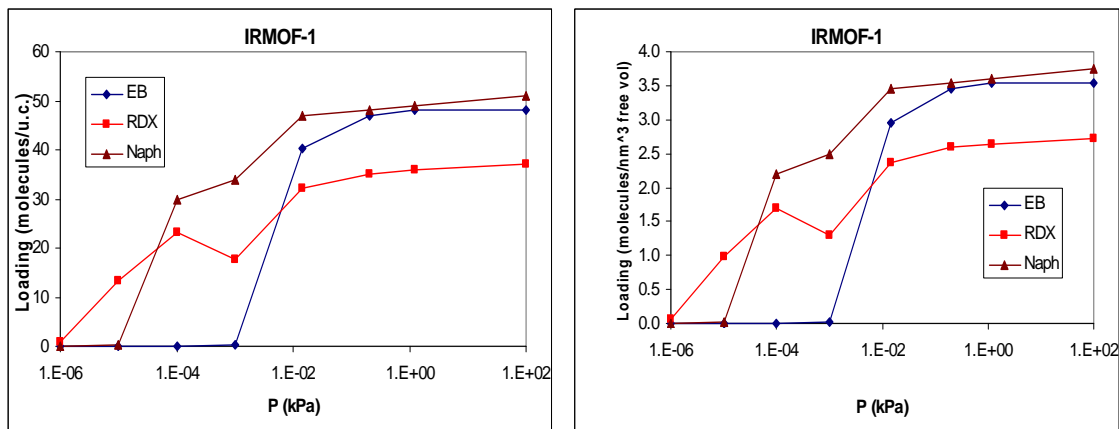
Figure 13. Comparison of the adsorption isotherms predicted for ethylbenzene (EB), the explosive RDX, and naphthalene. Curves on the left correspond to loading in units of mg g^{-1} of MOF, while those on the right are in units of molecules nm^{-3} pore volume.

References

1. Duren, T.; Sarkisov, L.; Yaghi, O. M.; Snurr, R. Q. *Langmuir* **2004**, 20, 2683.
2. Garberoglio, G.; Skoulidas, A. I.; Johnson, J. K. *J. Phys. Chem. B* **2005**, 109, 13094.
3. Connolly, M. L. Science **1983**, 221, 709.
4. Eddaoudi, M.; Kim, J.; Rosi, N.; Vodak, D.; Wachter, J.; O'Keefe, M.; Yaghi, O. M. *Science* **2002**, 295, 469.
5. Chui, S. S. Y.; Lo, S. M. F.; Charmant, J. P. H.; Orpen, A. G.; Williams, I. D. *Science* **1999**, 283, 1148.
6. Millange, F.; Serre, C.; Ferey, G. *Chemical Communications* **2002**, 822.
7. Dubbeldam, D.; Walton, K. S.; Ellis, D. E.; Snurr, R. Q. *Angew. Chem. Int. Ed.* **2007**, 46, 4496.
8. Dauber-Osguthorpe, P.; Roberts, V. A.; Osguthorpe, D. J.; Wolff, J.; Genest, M.; Hagler, A. T. *Proteins: Struct., Funct., Genet.* **1988**, 4, 31.
9. Yang, Q. Y.; Zhong, C. L. *J. Phys. Chem. B* **2006**, 110, 17776.
10. Coombes, D. S.; Cora, F.; Mellot-Draznieks, C.; Bell, R. G. *J. Phys. Chem. C* **2009**, 113, 544.
11. Berendsen, H. J. C.; Postma, J. P. M.; von Gunsteren, W. F.; Hermans, J. *In Intermolecular Forces*; Pullman, B., Ed.; Reidel: Dordrecht, Holland, **1981**; pp 331.

[Blank page following section.]

5. SUMMARY OF RESULTS OF COMSOL MODELING OF MICROCANTILEVER RESPONSE

5.1 Introduction

Device sensitivity can be maximized by both design modifications and selection of materials with appropriate mechanical properties. In this section, we describe a simplified model of a MOF-coated microcantilever. The effects of silicon doping and orientation on the sensitivity are described. In addition, the effects of MOF layer thickness and Young's modulus are examined. The impact of changing the dielectric layer from silica to silicon nitride beneath the MOF layer was also modeled.

5.2 Results

A simplified cantilever geometry was modeled with COMSOL, in which a single crystal silicon strain gauge is positioned on top of a silica beam of uniform composition (Fig. 14). The crystallographic directional properties including the Young's Modulus and piezoelectric constants of silicon are included in the model. The effects of changing the orientation of the cantilever on the (100) silicon wafer and effect of doping n or p-type silicon was investigated for a beam of dimensions of 250 μm length, 100 μm width and 1 μm thickness. The surface stress was simulated by applying a edge load of 1N/m on the perimeter at the top of the silica layer on the beam.
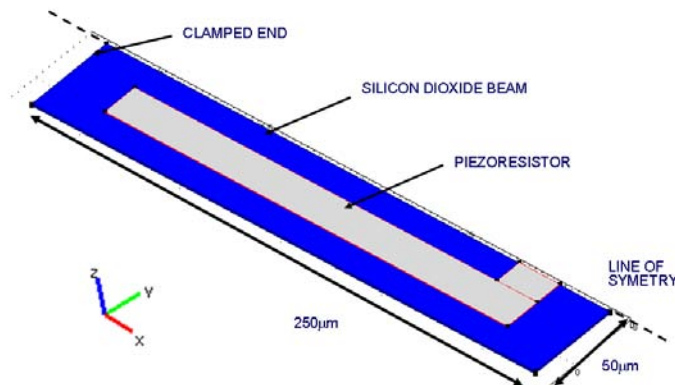
Figure 14. Schematic diagram of beam geometry. Note only one half is modeled due to line of symmetry in center of beam.
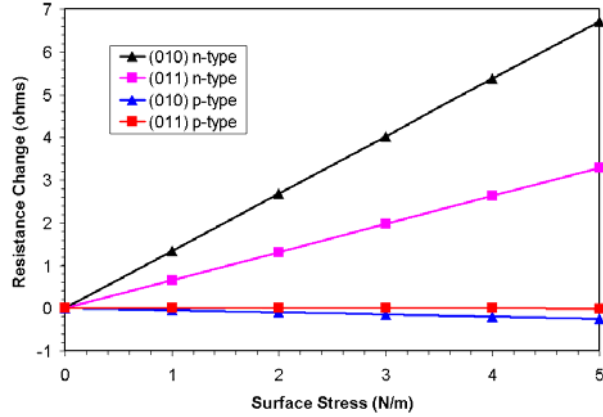
Figure 15. The effect of doping and silicon orientation on the response to surface stress 1N/m.

In figure 15 is it clear that n-type doping has a higher sensitivity to stress than p-type which is the normally used doping in strain gauges for commercially available AFM probes. Also, the use of beams aligned to the (010) direction of the silicon will be approximately twice as sensitive as beams aligned in the (011) direction. Our current experiments are being conducted with beams aligned parallel to the wafer flat which is the (011) direction.

The second model which represents just one half of the beam including the silicon strain gauge and with the additional area of the beam removed. The total length was 100 μm, total thickness 2.02 μm and width 40 μm. The model includes the MOF film of thickness 340 nm on top of a 340 nm of dielectric film, 340 nm of silicon and 1 μm of silica (total of 2.02 μm).

The effects of variation in the thickness and Young's Modulus of the MOF layer on the sensor response was examined. The effect of the properties of the dielectric layer was examined and the effect of the cantilever thickness. The strain in the MOF film is simulated by assuming a temperature expansion coefficient of 1×10^{-5} /^{o}C in the MOF layer and introducing a temperature change of 100^oC, while all other layers have a zero expansion coefficient. The resultant strain is 0.1% in the MOF layer.

Figure 16 shows the effect of the Young's Modulus of the MOF film. Note the large stress is present in the case where a higher modulus is present. This appears reasonable as the stiffer MOF produces a large bending moment for the same strain value in each case.

42
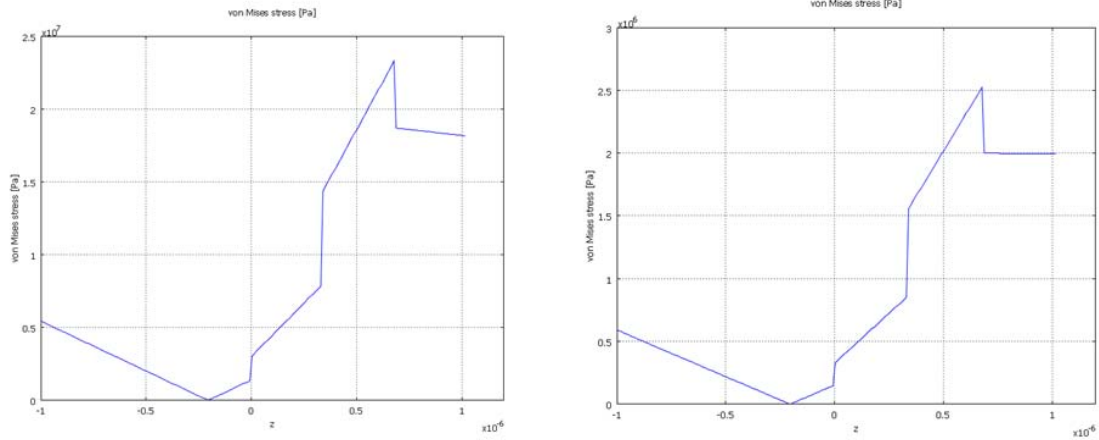
Figure 16. (left) Young's modulus of 13.5GPa, (right) Young's modulus of 1.35GPa.

Figure 17 shows the effect of changing the dielectric layer from silica to silicon nitride beneath the MOF layer. Improved coupling of the stress to the silicon strain gauge layer is observed. This layer thickness and properties should be carefully selected to provide electrical insulation and optimum stress coupling.
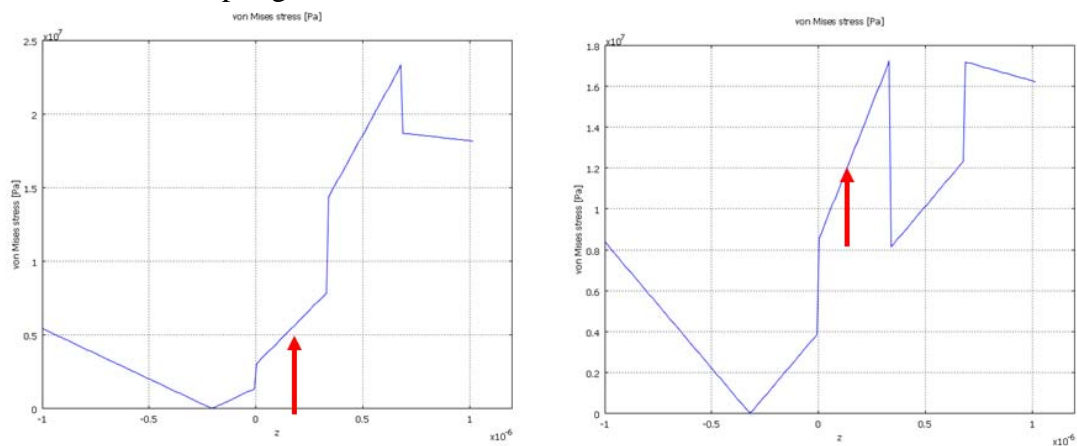
Figure 17. The von Mises stress as a function of position through the thickness of the beam. The red arrow indicated the middle of the silicon strain gauge.

Figure 18 shows the effect of MOF layer thickness on the sensor response for a silica thickness of 0.5 μm and 340 nm silicon dioxide dielectric layer beneath the MOF. Clearly more MOF produces a higher response for the same amount of strain. To produce that strain with more MOF the amount of adsorbed chemical would necessary increase; however the concentration in gas phase would be unchanged.
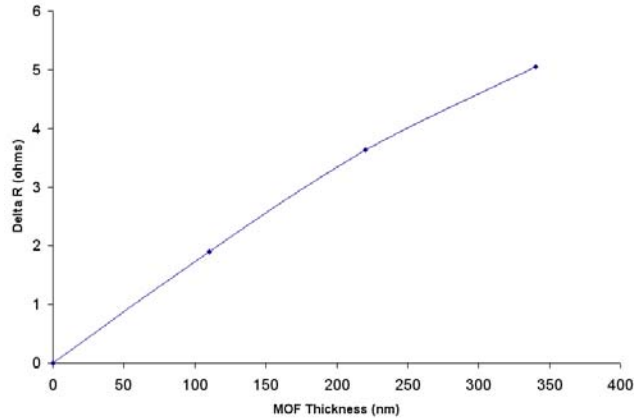
Figure 18. Effect of MOF layer thickness on the sensor response.

The effect of the silica layer thickness was examined for 0.25 μm, 0.5 μm and 1 μm and the results indicated a very minor change in sensitivity with thickness. This suggests more work is needed to understand if there is an optimum ratio between the thicknesses of the silicon dioxide layer under the MOF compared to the silica layer under the silicon strain gauge.

In addition, further work in needed to examine the effect of mesh size on the results, as this data has not been compared against an analytical model for the beam response to surface stress. Purely qualitative conclusions can only be drawn until the model has been benchmarked against an independent analytical calculation.

In summary:

1. Silica beams are more sensitive than silicon nitride beams.
2. p-doped (010)-oriented silicon is more sensitive.
3. Increasing the MOF thickness increases the sensitivity.
4. MOFs with higher Young's Modulus are preferred.

APPENDIX A

Supporting Information
HKUST-1 Thin film Growth Procedure

General

Solvents were purchased from Fisher and used without further purification. Copper (II) acetate and 11-mercaptoundecanoic acid were purchased from Aldrich and trimesic acid was purchased from Fluka. All reagents were used without further purification.

Step-by-Step Growth

Single-crystalline silicon wafers sputter coated with ~2nm Ti followed by ~100 nm Au(111) were cleaned by immersion in acetic acid for 5-10 min followed by rinsing with pure ethanol and drying under a N_2 stream. The Au-substrates were then immersed in a 20 mM solution of 11-mercaptoundecanoic acid (25 mg in 5 mL ethanol + 500 μL acetic acid) for 20 hours. The substrates were then removed, rinsed thoroughly with ethanol, and dried under a N_2 stream. The substrates were then iteratively immersed in separate 1 mM ethanolic solutions of copper (II) acetate (2 mg in 10 mL; 30 min submersion) and trimesic acid (2 mg in 10 mL; 60 min submersion). Between each immersion, the substrate was rinsed thoroughly with ethanol and dried under a N_2 stream. Typical substrates underwent 20 cycles of growth.

Single Step in situ *Growth*: SAM@Au(111) substrates were cleaned and prepared as aboveThe HKUST-1 growth solution was prepared by dissolving $Cu(NO_3)_2 \cdot 3H_2O$ (1.48 g; 6 mmol) in 15 mL water and trimesic acid (845 mg; 4 mmol) in 15 mL ethanol. The two solutions were mixed together and placed in an oven at 80 °C for 3 days. The growth solution was removed from the oven and placed in an ice-water bath for 10 min. The mother liquor was then filtered through a 0.2 μm PES membrane filter. The substrates were placed face down or vertical in the filtered growth solution for 5 days. There was no appreciable difference in film growth between the vertically and face down substrates. The films were characterized by Raman and pXRD.

MOF Growth on Microcantilevers

The method for growth on a cantilever chip is analogous to the bulk substrates; however the volume of each solution is increased to 30 mL to accommodate the physical height of the chip from the base of the electronics package when mounted. Also the N_2-stream drying step was omitted due to the fragility of the cantilevers. The dimensions of individual microcantilevers were 200 μm long x 40 μm wide x 1 μm thick.

Raman Spectroscopy and Silver Evaporation for SERS Enhancement

Raman spectra were collected on an Acton SpectraPro model 2750 0.75 m triple spectrometer, with a Spectra Physics diode pumped and frequency doubled Nd:YAG 532 nm laser as the excitation source at a power of ~0.5 mW at the sample. All spectra were taken with a microprobe apparatus consisting of a 20× objective to focus the incident light to a spot of ~2 μm^2 and collect the scattered light in 180° backscattering geometry. Silver was evaporated using a CHA Autotech II electron beam evaporator at a vacuum of 10^{-6} Torr, a rate of 0.7 Å/sec, and an equivalent thickness of 25 Å based on a quartz crystal monitor. The sample was held at room temperature.

Gas testing

The response of the MOF-coated sensor to analytes was determined by mounting the cantilever array within a cell through which gases or liquid vapors in dry N_2 flowed at atmospheric pressure. The measurement and reference cantilevers were connected in a Wheatstone bridge, excited by a 1 kHz AC signal, and a lock-in amplifier was used to measure the bridge output with an integration time of 1 s.
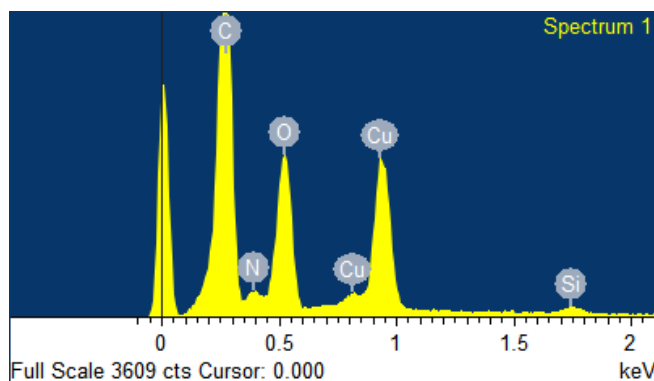
Spectrum processing :
No peaks omitted

Processing option : All elements analyzed (Normalised)
Number of iterations = 3

Standard :
C   CaCO3   1-Jun-1999 12:00 AM
N   Not defined   1-Jun-1999 12:00 AM
O   SiO2   1-Jun-1999 12:00 AM
Si   SiO2   1-Jun-1999 12:00 AM
Cu   Cu   1-Jun-1999 12:00 AM

Element	Weight %	Atomic %
C K	36.61	58.12
N K	4.15	5.64
O K	20.13	23.99
Si K	1.34	0.91
Cu L	37.77	11.33
Totals	100.00	

Figure S1: Electron Dispersive X-ray spectral data from a portion of the testing cantilever showing the proper atomic percentages of copper and carbon. Oxygen and nitrogen values cannot be trusted due to the large penetration depth of the analysis method and the presence of both silicon nitride and silica layers below the MOF layer.

Chemical Characterization of HKUST-1 Films
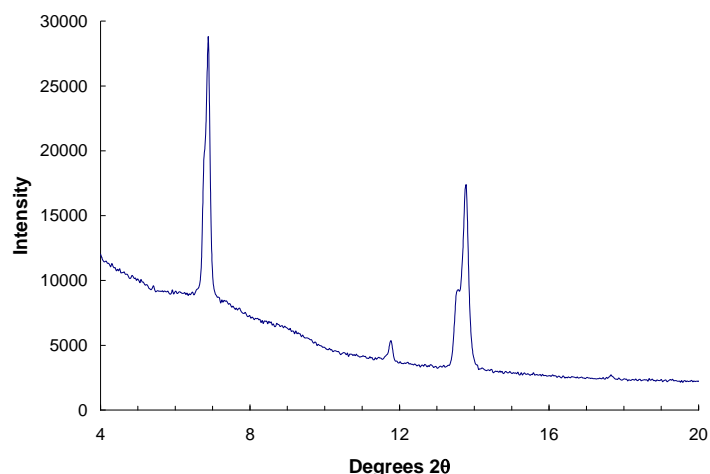
Figure S2: Powder X-ray diffraction pattern of HKUST-1 grown on a SAM@Au substrate *via* the single step *in situ* growth method. As expected, the pattern indicates the highly oriented growth mode observed by Biemmi *et al.*(ref. 8) for a COOH-terminated SAM on Au.
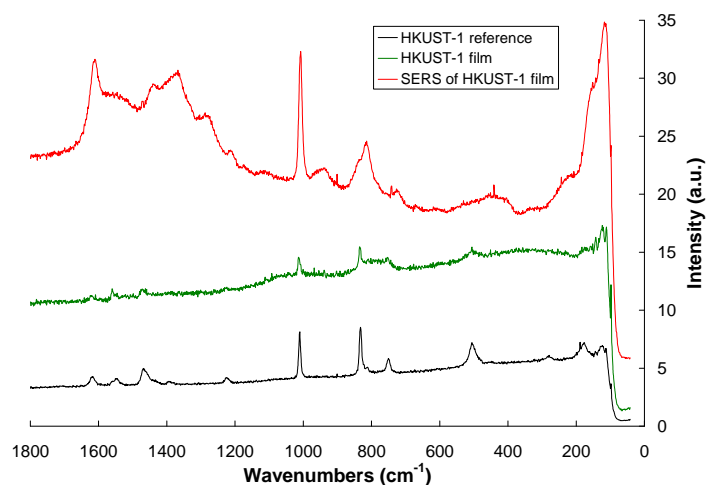
Figure S3: Micro Raman spectra of the HKUST-1 reference film (black; see also **Fig. 1**), which was grown on a macroscopic substrate prior to enhancement via Ag deposition (green), and the same HKUST-1 film post-Ag deposition showing SERS activity (red; see **Fig. 1**). Both unenhanced spectra (black and green) show the resonances characteristic of HKUST-1 at 1620, 1550, 1470, 1230, 1010, 832, 750, 507 and 180 cm^{-1}. (Prestipino *et al.*, ref. 12.) The SERS spectrum retains many of the key features (1610, 1010, 832-750, 180 cm^{-1}). Small frequency shifts and differences in intensity are expected, since the mechanism of SERS differs from that of unenhanced Raman spectroscopy.

47

A)

B)

C)

D)
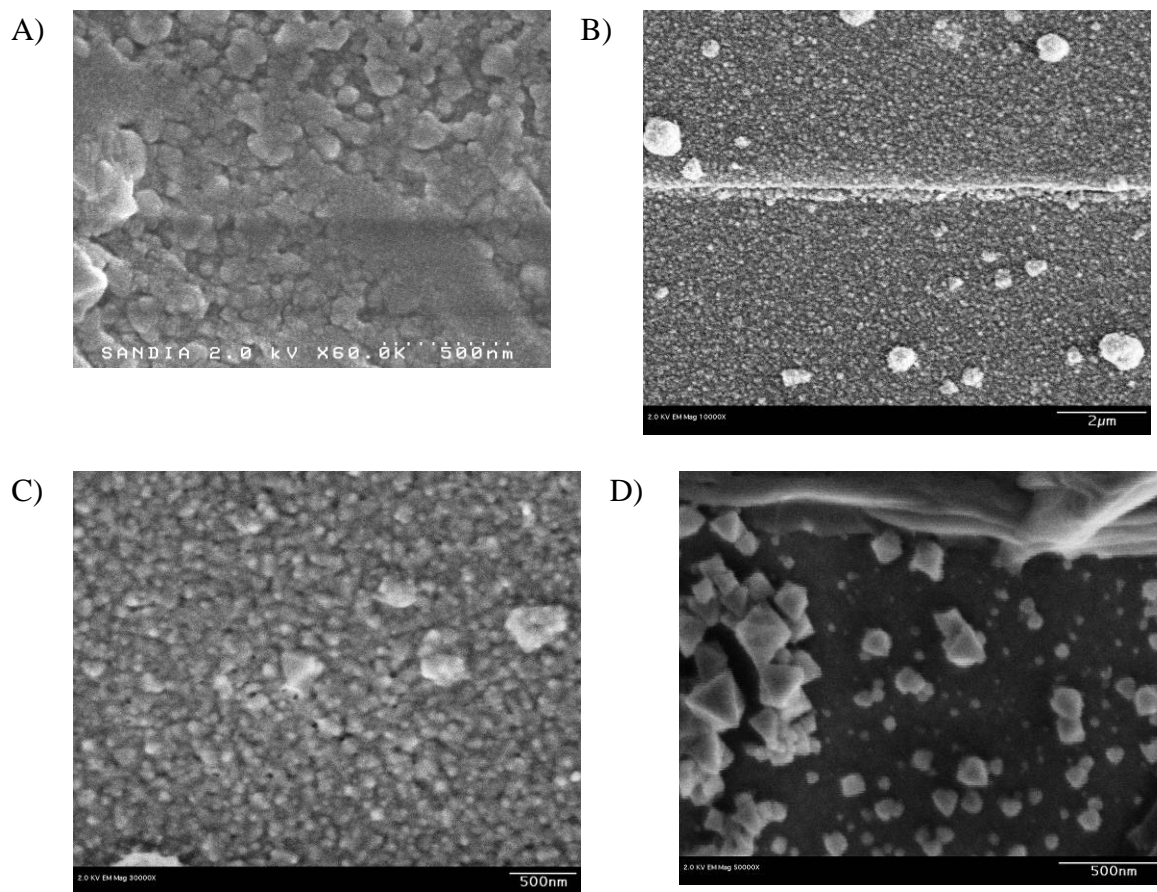
Figure S4: Scanning electron micrographs of HKUST-1 films grown by the step-by-step method on microcantilevers, showing the range of morphologies obtained. These different morphologies are similar to those reported by Wang et al. (Ref. 13). A) 60kx. In this film the images exhibit feature sizes less than 100nm for the majority of the coating B) 20kx. In this film, the horizontal line is one of the gold lines used to supply current to the piezoresistive sensor. C) Same film as in (B), but at 60 kx. (D) A third film; 30 kx. In this case, what appear to be amorphous structures are found in some places on the surface, as seen at the top of the image.

Estimation of strain in microcantilevers

The stress in the MOF layer is computed from the theory for a composite beam under linear elastic deformation with isotropic properties [S. Huang, X. Zhang, *J. Micromech. Microeng.* **16**, 382 (2006)]. The bending is assumed to be produced by the difference in the volumetric expansion of one of the layers in the beam with respect to the other components. The neutral axis is calculated for the composite beam given published mechanical properties of the layers [G. Kovacs, Transducers Handbook, McGraw Hill, 1999], and our value for the Young's modulus of the MOF material of 18.5GPa, obtained from nanoindentation measurements. The relevant equations for calculation of the strain in the silicon layer are given by:

$$\varepsilon_{Si} = \frac{\Delta R / R}{E_{Si}\pi_{\exp}} \quad \text{and hence the strain in the MOF film is given by: } \varepsilon_{mof} = \varepsilon_{Si}\frac{(h_{mof} - z_0)}{(h_{Si} - z_0)}$$

R is the maximum resistance change at saturation, R is the resistance of the piezoresistive gauge, E_{Si} is the Young's Modulus of single-crystal silicon, $_{\exp}$ is the experimentally determined piezoresitive coefficient, $_{Si}$ is the strain in the silicon, h_{mof} is the mid-height of the MOF film, and h_{Si} is the height of the middle of the silicon strain gauge. The neutral axis, z_0, is calculated from the extensional stiffness (A), flexural-extensional coupling (B), flexural stiffness coefficients (D), axial force (N), and bending moment (M):

$$z_0 = \frac{DN - BM}{BN - AM} \quad A = \int_0^h E(z)dz \quad B = \int_0^h E(z)zdz \quad D = \int_0^h E(z)z^2dz \quad N = \int_0^h E(z)\varepsilon(z)dz \quad \text{and}$$

$$M = \int_0^h E(z)\varepsilon(z)zdz$$

where h is the total beam thickness. To compute the strain induced in the MOF layer, we first compute the piezoresistive coefficient $_{\exp}$ for the cantilever, which relates the measured resistance change to the force applied to the beam. The maximum resistance change observed here, 5-ohms, corresponds to a strain in the silicon layer of 0.0075% which would be produced by a strain of 0.012% in the MOF film. This calculation is based upon a measured piezoresistive coefficient of $20\times10^{-11} \pm 5\times10^{-11}$/Pa for the beam, which was determined with an AFM to produce a calibrated deflection of the beam. This value is lower than the published of 50×10^{-11} / Pa [O.N. Tufte, E. L. Stelzer, *Physical Review A* **166**, 1707 (1964)] that can result in single crystal n-type silicon for uniform plane strain. The difference is probably due to the assumptions of uniform doping and strain uniformity. In our experiment ion-implantation was used to form the strain gauge. As a result, the doping is a function of depth, which will result in a location-dependant coefficient. In addition, x-axis strain may be dominant due to the high aspect ratio of the beam, which will lower the coefficient.

The thicknesses of the various layers in the cantilever are shown in Figure S5. The following constants assumed in the calculation are given in Tables S1 – S3:

Table S1: Tested Beam Dimensions

Length	200	um
Thickness	1.1	um
Width	40	um
Location of gauge	0.75	um
Bridge voltage	1	V
Beam Resistance Value	2050	ohms

Table S2: Beam Effective Modulus

	108.2273	Gpa
Modulus of MOF	18.5	GPa
Modulus of Silicon	160	GPa
Mod of Nitride	140	GPa
Mod of Silicon Oxide	68	GPa
Poisson Ratio	0.3	

Table S3: Predicted stress and strain values

|		
Observed resistance change	5	ohms
Stress produced	0.01196	Gpa
Total strain produced	0.00748	%
Strain in MOF layer	0.01215	%

Fitting the resistance vs. concentration curves for both the hydrated and dehydrated sensors yields a resistance change at saturation of 7.0 ohms (see below). Scaling the computed strain to the saturation resistance value yields a maximum strain of $0.0171 \pm 0.003\%$.

The expansion of the unit-cell dimension of the HKUST-1 unit cell upon complete hydration obtained from x-ray diffraction is 0.45% [C. Prestipino et al. *Chem. Mater.* **2006**, *18*, 1337], which equates to a strain of the same amount. This value is higher than that measured on the cantilever beam, due most likely to several factors: First, the MOF coating may not be completely uniform, resulting in areas with lower strain. Second, the coupling of the MOF coating to the silicon nitride surface via a self assembled monolayer on gold is not expected to be a rigid mechanical coupling, which will also reduce the strain produced in the cantilever beam. Third, because the coating is polycrystalline, grain boundaries exist within the film that may absorb some of the stress. Finally, Figure 3 indicates that the sensor is not fully saturated in our experiments.
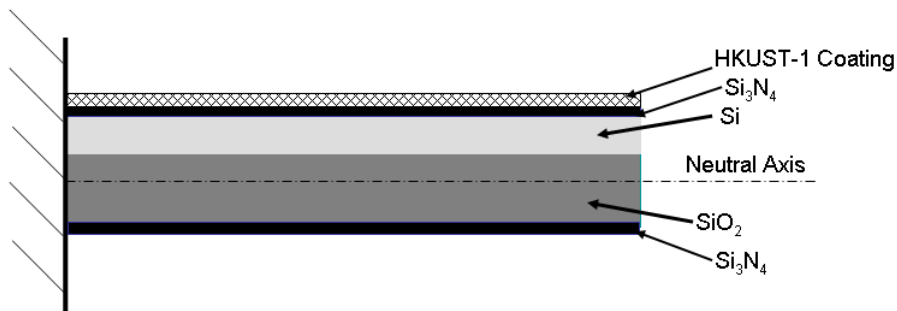
Figure S5: Schematic of the microcantilever used in these experiments. The thicknesses of the different materials are: MOF coating: 0.1 μm, Si_3N_4: 0.1μm; Si: 0.3 μm; SiO_2: 0.4 μm; bottom Si_3N_4: 0.2 μm.

Langmuir isotherm fits of the H_2O resistance vs. partial pressure curves
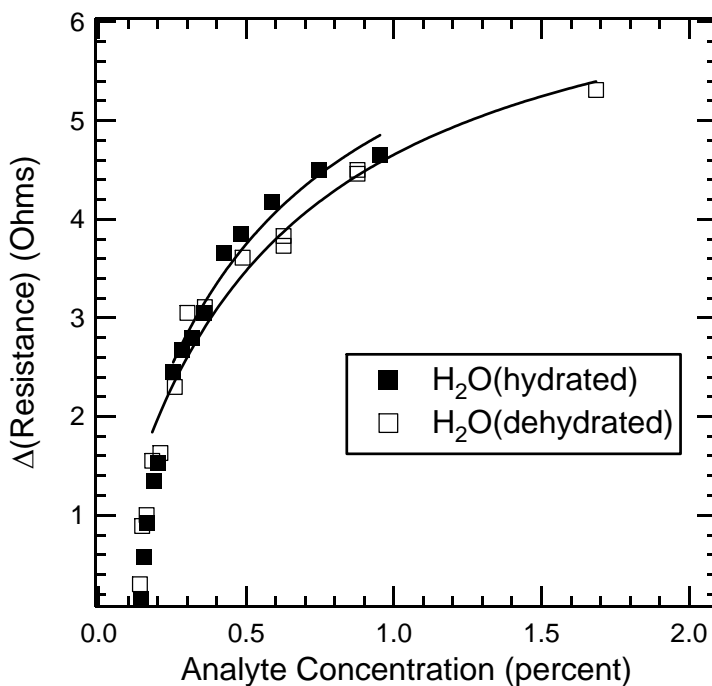
Figure S6. Fit of a Langmuir isotherm to resistance vs. concentration data for H_2O. Data at the lowest concentrations (yielding resistances < 1.0 ohm) do not fit well to a single isotherm over the entire analyte range. This is most likely primarily due to the limited accuracy of the flow controller, which was at the low end of its range at these low flow rates.

[Blank page following section.]

APPENDIX B

Force Field Validation for Molecular Dynamics Simulations of IRMOF-1 and Other Isoreticular Zinc Carboxylate Coordination Polymers

Jeffery A. Greathouse*[†] and Mark D. Allendorf[‡]
[†]Geochemistry Department, Sandia National Laboratories, Albuquerque, New Mexico, 87185-0754. [‡]Microfluidics Department, Sandia National Laboratories, Livermore, California, 94551
*E-mail: jagreat@sandia.gov

Supporting Information

1. Calculation of the Bulk modulus of IRMOF-1.

Plot: MD Simulation, 300 K

$y = -206.7 + 371.5x^2 - 1202.2x^3 - 2.811 \times 105x^4$

$B_0 = 4.04$ GPa

Y-axis: U (MJ/mol), values from -206.60 to -206.70

X-axis: $(V_0/V)^{2/3} - 1$, values from -0.02 to 0.02
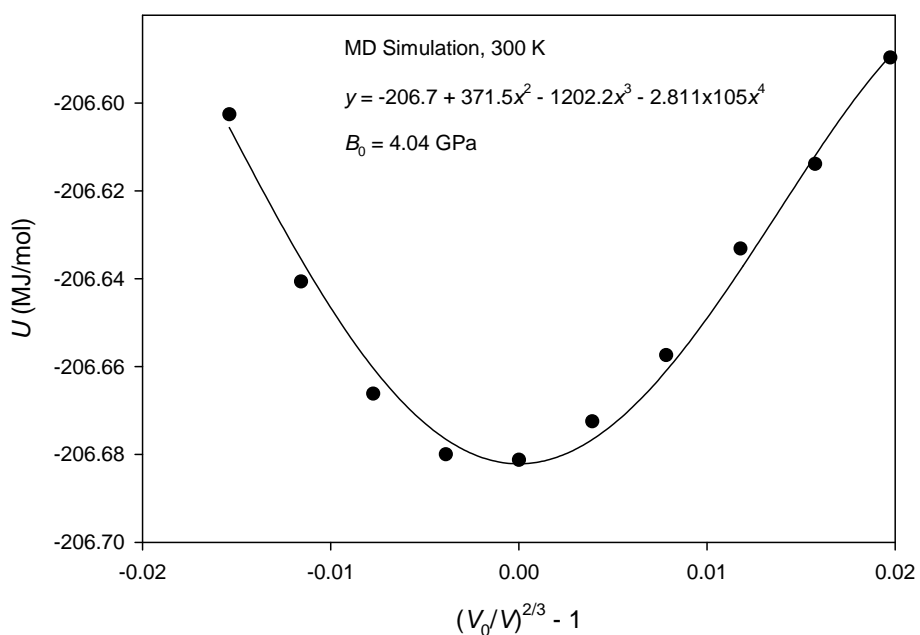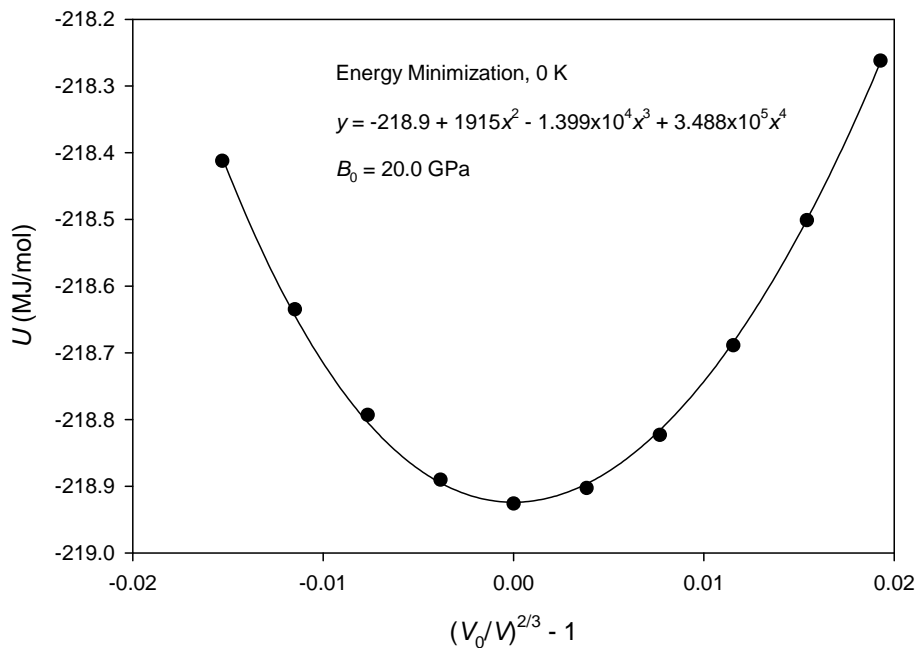
Figure SI-1. Energy-volume graphs used to obtain the bulk modulus (B_0) from MD simulation at 300 K (top) and energy minimization at 0 K (bottom). The quantities U, V_0, and V represent the potential energy, equilibrium volume, and strained volume, respectively. Symbols represent the simulation data points, and the line represents the regression fit given by the equation.

2. Calculation of the Young's modulus of IRMOF-1.

MD Simulation, 300 K

$y = 7.433x^2 + 32.75$

$E_0 = 14.87$ GPa

Energy Minimization, 0 K

$y = 17.76x^2 - 66.76$

$E_0 = 35.53$ GPa
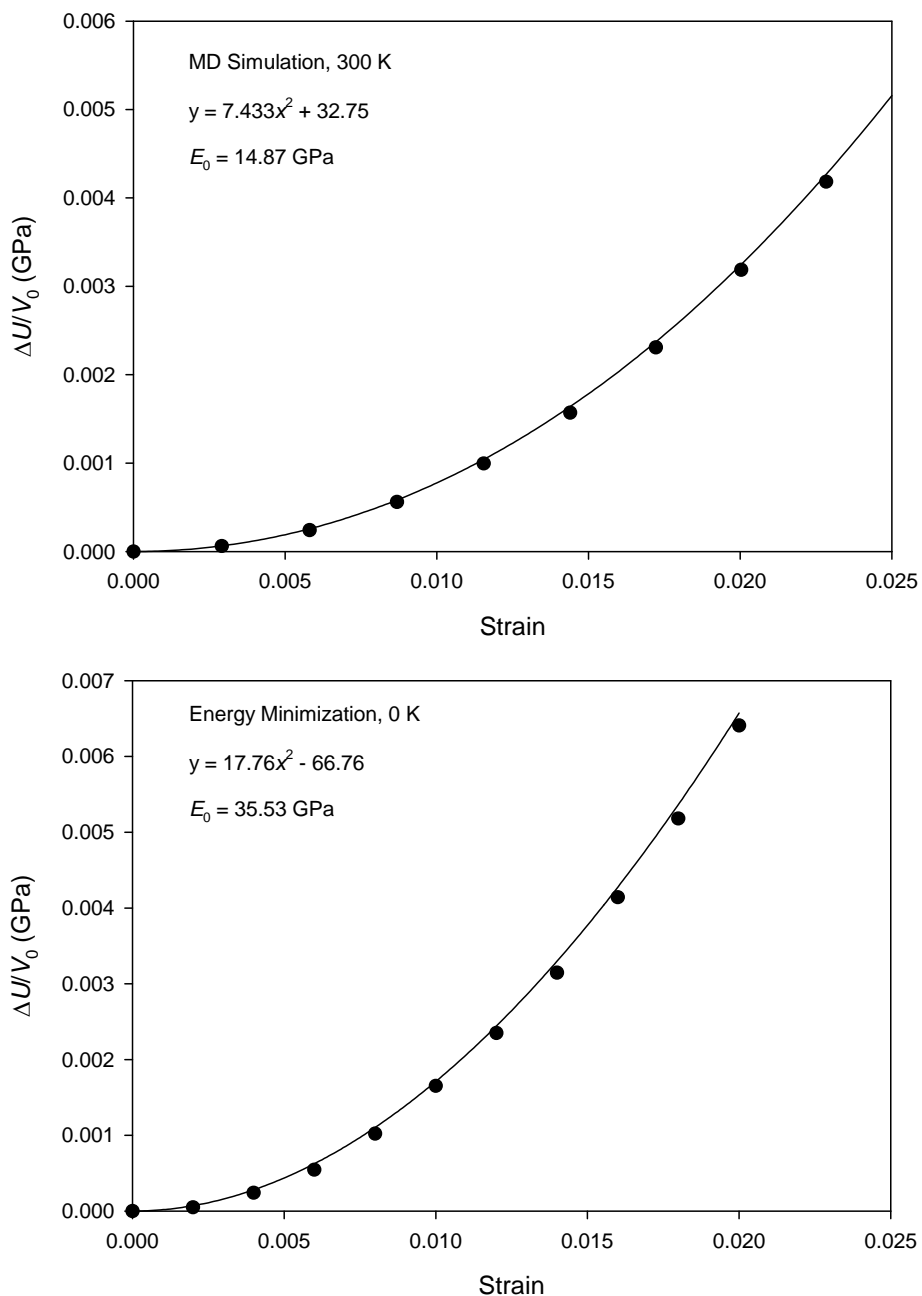
Figure SI-2. Energy-strain graphs used to obtain the Young's modulus (E_0) from MD simulation at 300 K (top) and energy minimization at 0 K (bottom). The strain load is obtained from the strained lattice parameter *l* and equilibrium lattice parameter l_0 by $(l - l_0)/l$. Symbols represent the simulation data points, and the line represents the regression fit given by the equation.

3. Animation results for IRMOF-1, simulation at 400 K (see corresponding AVI file).

The animation represents 200 ps of simulation time. The benzene dicarboxylate molecule rotates such that the $Zn\text{-}O_{carb}$ bonds are not broken. The rotation takes place about $C_{phenyl}\text{-}C_{carb}$ bonds. Atoms are colored as follows: C (gray), O (red), Zn (blue), H (white). Atoms colored in green represent O_{carb}, C_{phenyl}, and H atoms that are initially on the same side of the molecule.

APPENDIX C

Publications, Presentations, and Intellectual Property

Journal articles

1. M. D. Allendorf, R. J. T. Houk, L. Andruszkiewicz, A. A. Talin, J. Pikarsky, A. Choudhury, K. A. Gall, and P. J. Hesketh "Stress-Induced Chemical Detection Using Flexible Metal-Organic Frameworks" *J. Amer. Chem. Soc.,* 130 **2008**, 14404.
2. J. A. Greathouse, T. L. Kinnibrugh, and M. D. Allendorf "Adsorption and Separation of Noble Gases by IRMOF-1: Grand Canonical Monte Carlo Simulations" *Ind. Eng. Chem. Res.,* 48 **2009**, 3425-3431.
3. J. A. Greathouse, M. D. Allendorf "Force field validation for molecular dynamics simulations of IRMOF-1 and other isoreticular zinc carboxylate coordination polymers" *J. Phys. Chem. C*. 112 **2008**, 5795-5802.
4. J. A. Greathouse and M. D. Allendorf, "Low pressure adsorption of large organics by metal-organic frameworks: A computational screening study" submitted to *Chem. Mater.* September **2009**.

Reviewed conference proceedings

1. P. J. Hesketh, L. Andruszkiewicz, Xaihui Lin, A. Choudhury, M. Allendorf "Microfabricated Cantilever Sensors and Microfluidic Packaging for Sensors," Proceedings of ICMEMS Meeting, Madras India, January 2-5, 2009, 5 pgs.
2. R. J. T. Houk, J. H. Lee, M. D. Allendorf, P. J. Hesketh "The Metal-Organic Films for Tailorable Chemical Sensing on Microcantilevers" Transactions of the ECS, Vol. 19, No. 6, pp. 267-278 (2009).

Conference presentations

1. Invited opening plenary: M. D. Allendorf, R. J. T. Houk, P. Doty, N. Chang, Raghu Bhakta, Ben Jacobs, and Peter Hesketh "Chemical and radiation sensing using metal-organic frameworks" MOFCATS Workshop, Oslo, Norway June 17 – 19, 2009.
2. Invited seminar: P. J. Hesketh "Metal-Organic Framework Coated Microcantilever Sensors for Chemical Sensing and Nanocantilever Chem/Biosensors" seminar at Oak Ridge National Laboratories, June 15, 2009.
3. R. J. T. Houk, J. Lee, P. J. Hesketh, M. D. Allendorf, "Metal-Organic Frameworks Tailorable Nanoporous Materials for Chemical Sensing" ECS Meeting, San Francisco, May 2009.
4. M. D. Allendorf, R. J. T. Houk, L. Andreszkiewicz, A. A. Talin, P. J. Hesketh, "MEMS-Based Microcantilever Sensors Using Nanoporous Metal-Organic Frameworks for Chemical Monitoring" ECS Meeting, San Francisco, May 2009.
5. Invited presentation: M. D. Allendorf, R. J. T. Houk, L. Andreszkiewicz, A. A. Talin, P. J. Hesketh, "Chemical Detection Using Metal-Organic Frameworks" SPIE Defense, Security, and Sensing Conference, Orlando, April 2009.

6. Invited seminar: P. J. Hesketh "Microcantilever Chemical Sensing with MOF's" seminar at Clemson University, February 13, 2009.
7. Plenary lecture: P. J. Hesketh, "Microfabricated Cantilever Sensors and Microfluidic Packaging for Sensors" ICMEMS Meeting, Madras, India, January 2-5, 2009.
8. Invited seminar: M. D. Allendorf "Metal Organic Frameworks: Novel Nanoporous Materials for Sensing Applications" seminar at Dept. of Electrical Engineering and Computer Science, University of California, Berkeley, April 18, 2008.
9. J. A. Greathouse, T. L. Kinnibrugh, M. D. Allendorf "Molecular simulation of gas adsorption in IRMOF-1 using a flexible force field" spring meeting of The American Chemical Society, New Orleans, LA April 6 – 10, 2008.
10. J. A. Greathouse, T. L. Kinnibrugh, F. P. Doty, and M. D. Allendorf "Molecular Modeling of Gas Adsorption in Scintillating Metal-Organic Frameworks" Fall MRS meeting, Boston, MA, November 26 – 30, 2007.
11. A. Choudhury, P. Hesketh, Z. Hu, T. Thundat, R. Bhakta, R. Houk, A. Skulan, G. Aigeldinger, A. Talin and M. Allendorf "Chemical Detection with MOF-Functionalized Piezoresistive Microcantilever Arrays" ECS Washington DC meeting, October 2007.
12. Invited presentation: M. D. Allendorf, J. A. Greathouse, T. L. Kinnibrugh, "Force Field Validation for Molecular Simulations of IRMOF-1 and Other Isoreticular Zinc Carboxylate Coordination Polymers" CECAM conference, Lyon, France July 15 – 18, 2007.
13. P. Hesketh, A. Choudhury, R. Luharuka, Z. Hu, T. Thundat, M. D. Allendorf "Microfabricated Cantilever Arrays and Miniature Bistable Rotary Gate Valves for Chemical Sensing" International Conference on Materials for Advanced Technologies, Singapore, July 1 – 6, 2007.
14. J. A. Greathouse, M. D. Allendorf "Validation of a Nonbonded Force Field for Metal-Organic Frameworks" presented in Nanoporous Materials: Chemistry and Applications symposium held at The Electrochemical Society Spring Meeting, Chicago, IL, May 7 – 11, 2007.
15. M. D. Allendorf "Metal Organic Frameworks: Nanoporous Materials for Sensing, Separations, and More," ECS San Francisco Section meeting, Oakland, CA, February 13, 2007.

Inventions

1. P. J. Hesketh, M. D. Allendorf "High temperature microcantilever sensors," Invention disclosure #4826, April 2009.

DISTRIBUTION

Sandia National Laboratories